

Probing Physics Beyond the Standard Model through Combined Analyses of Next-Generation Type Ia Supernova, CMB, and BAO Surveys

SRINIVASAN RAGHUNATHAN,^{1,2} AYAN MITRA,² NIKOLINA ŠARČEVIĆ,³ FEI GE,^{4,5,6} CORENTIN RAVOUX,⁷
CHRISTOS GEORGIU,⁸ RENÉE HLOŽEK,^{9,10} RICHARD KESSLER,^{11,12} GAUTHAM NARAYAN,^{13,2} PAUL ROGOZENSKI,¹⁴
PAUL SHAH,¹⁵ GEORGIOS VALOGIANNIS^{12,11} AND JOAQUIN VIEIRA^{13,16,2}

(THE LSST DARK ENERGY SCIENCE COLLABORATION)

¹*Department of Physics, University of California, One Shields Avenue, Davis, CA, 95616, USA*

²*Center for AstroPhysical Surveys, National Center for Supercomputing Applications, Urbana, IL, 61801, USA*

³*Department of Physics, Duke University, Durham NC 27708, USA*

⁴*California Institute of Technology, 1200 East California Boulevard., Pasadena, CA, 91125, USA*

⁵*Kavli Institute for Particle Astrophysics and Cosmology, 382 Via Pueblo Mall, Stanford, California 94305-4060, USA*

⁶*SLAC National Accelerator Laboratory, 2575 Sand Hill Road, Menlo Park, California 94025, USA*

⁷*Université Clermont Auvergne, CNRS, LPCA, 63000 Clermont-Ferrand, France*

⁸*Institut de Física d'Altes Energies (IFAE), The Barcelona Institute of Science and Technology, Campus UAB, 08193 Bellaterra (Barcelona), Spain*

⁹*Dunlap Institute for Astronomy and Astrophysics, University of Toronto, Toronto, ON, CA*

¹⁰*David A. Dunlap Department of Astronomy and Astrophysics, University of Toronto, Toronto, ON, CA*

¹¹*Kavli Institute for Cosmological Physics, University of Chicago, Chicago, IL 60637, USA*

¹²*Department of Astronomy and Astrophysics, University of Chicago, 5640 South Ellis Avenue, Chicago, IL 60637, USA*

¹³*Department of Astronomy, University of Illinois Urbana-Champaign, 1002 West Green Street, Urbana, IL, 61801, USA*

¹⁴*McWilliams Center for Cosmology and Astrophysics, Department of Physics, Carnegie Mellon University, Pittsburgh, PA 15213, USA*

¹⁵*Department of Physics & Astronomy, University College London, Gower Street, London, WC1E 6BT, UK*

¹⁶*Department of Physics, University of Illinois Urbana-Champaign, 1110 West Green Street, Urbana, IL, 61801, USA*

ABSTRACT

Observations of Type Ia supernovae (SNIa), baryon acoustic oscillations (BAO), and the cosmic microwave background (CMB), which probe the late-, intermediate-, and early-universe epochs, respectively, provide complementary constraints on the expansion history of the Universe. In this work, we forecast constraints on dark energy and other extensions to the standard cosmological model by combining the SNIa sample expected from the Vera C. Rubin Observatory's Legacy Survey of Space and Time (LSST), data from current and forthcoming CMB surveys, and BAO measurements from the Dark Energy Spectroscopic Instrument (DESI). For the CMB, we use temperature, polarization, and lensing power spectra ($TT/EE/TE/\phi\phi$) from South Pole Telescope, the planned Advanced Simons Observatory, and a CMB-S4-like experiment. We derive constraints on Λ CDM and its extensions involving the dark energy equation of state parameters (w_0, w_a) and the sum of neutrino masses $\sum m_\nu$, using a Markov Chain Monte Carlo (MCMC) sampling framework. We find that the LSST Year-3 SNIa sample can improve upon the DES Year-5 dark energy constraints by a factor of $\times 2 - \times 2.5$, with the gains driven primarily by the significantly higher SNIa density in the LSST sample. Similarly, DESI-DR3 shows up to a $\times 1.8$ improvement on dark energy parameters over DR2, driven largely by the substantial increase in low-redshift sample. Combining CMB with LSST-Y3-SNIa and DESI-DR3-BAO yields $\sigma(w_0) = 0.028$ and $\sigma(w_a) = 0.11$ for $w_0 w_a$ CDM cosmology with the results being largely independent of the CMB dataset. The constraints weaken by 10%-30% when freeing $\sum m_\nu$ and spatial curvature. Moreover, the joint analysis of the three datasets can enable a $2 - 3\sigma$ detection of $\sum m_\nu$.

1. INTRODUCTION

The standard model of cosmology Λ CDM, has been extremely successful in describing the observations made by a variety of cosmological surveys. These observations include the temperature and polarization anisotropies of the cosmic microwave background (CMB, Planck Collaboration et al. 2020a; L. Balkenhol et al. 2021; T. Louis et al. 2025; E. Camphuis et al. 2025), CMB lensing (Y. Omori et al. 2017; Z. Pan et al. 2023; M. S. Madhavacheril et al. 2024; F. J. Qu et al. 2025), baryonic acoustic oscillations (BAO, S. Alam et al. 2021; DESI Collaboration et al. 2025), SNIa (A. G. Riess et al. 2022; DES Collaboration et al. 2024a; B. Popovic et al. 2025), galaxy clustering (S. Alam et al. 2017; C. Heymans et al. 2021; T. M. C. Abbott et al. 2022; H. Miyatake et al. 2023; A. G. Adame et al. 2025), galaxy weak lensing (S. Joudaki et al. 2020; Dark Energy Survey and Kilo-Degree Survey Collaboration 2023), and also cross-correlations between the above datasets (L. E. Bleem et al. 2012; T. Giannantonio et al. 2016; A. Krolewski et al. 2021; Y. Omori et al. 2023; S. Shaikh et al. 2024; M. A. Sabogal & R. C. Nunes 2025). However, the properties of the essential components that make up the model, namely dark matter and dark energy, remain poorly understood. Additionally, evidence for tensions between different cosmological probes (S. Joudaki et al. 2020; A. G. Riess et al. 2022; A. R. Khalife et al. 2024; DESI Collaboration et al. 2025; D. D. Y. Ong et al. 2026) has emerged over the past decade, driven by significant improvements in the measurement noise. Enormous efforts are underway across the community — from the observational side, aiming to identify systematics (K. Aylor et al. 2019; A. G. Riess et al. 2022, for example), to the theoretical side, exploring physics beyond the standard model (T. Karwal & M. Kamionkowski 2016; V. Poulin et al. 2019; M.-X. Lin et al. 2019; N. Schöneberg et al. 2019; L. Knox & M. Millea 2020; W. Elbers et al. 2025, for example) — to understand the origin of these tensions, albeit with only partial success. Subsequently, it is critical to use the observations from the current and upcoming state-of-the-art cosmological surveys to test the standard cosmological model to look for extensions as well as deviations.

In this work, we forecast the cosmological constraints from three probes of the cosmic expansion history expected from next-generation surveys. These include the Type Ia supernova (SNIa) sample anticipated from the

Vera C. Rubin Observatory’s Legacy Survey of Space and Time (LSST; LSST Science Collaboration et al. 2009; LSST Dark Energy Science Collaboration 2012); baryon acoustic oscillation (BAO) measurements from the Dark Energy Spectroscopic Instrument (DESI; DESI Collaboration et al. 2016); and measurements of the CMB from current and forthcoming surveys. Because they probe late-, intermediate-, and early-universe epochs, the three datasets provide distinct but highly complementary views of the expansion history.

For the SNIa dataset, we use the simulated LSST-Y3 sample containing the expected statistical and systematic errors for the distance modulus measurements designed for the Rubin LSST Dark Energy Science Collaboration (DESC¹, A. Mitra et al. 2023). For the CMB dataset, we use the temperature, polarization, and lensing power spectra ($TT/EE/TE/\phi\phi$) from the South Pole Telescope (SPT-3G, B. A. Benson et al. 2014; A. N. Bender et al. 2018); the enhanced configuration of the Simons Observatory (SO; The Simons Observatory Collaboration et al. 2018), referred to as Advanced-SO (ASO; The Simons Observatory Collaboration et al. 2025); and also a futuristic Stage-IV survey with specifications similar to the recently canceled CMB-S4 experiment (CMB-S4 Collaboration et al. 2016; CMB-S4 Collaboration 2019). We consider multiple survey options for each of the above CMB surveys, which we describe in the datasets section. Finally, for BAO, we consider multiple distance measurements from both the recently released DESI DR2 dataset (DESI Collaboration et al. 2025) and the upcoming mock DR3 data based on DESI Collaboration (2023).

The goal of this work can be decomposed into the following points:

- Compare forecasted constraints from the standard Fisher formalism with the results from Markov Chain Monte Carlo (MCMC) sampling for SNIa and CMB datasets.
- Study the impact of binning on cosmological constraints. Specifically, (a) to compare the constraints obtained when the CMB power spectra are binned with different values of Δ_ℓ with the unbinned case, and similarly (b) to compare the constraints obtained from the unbinned sample with the results when the SNIa sample is grouped in multiple redshift bins.
- Forecast and compare cosmological constraints using different combinations of CMB, SNIa, and

Corresponding author: Srinivasan Raghunathan
sriniraghuna@gmail.com

¹ <https://lsstdesc.org/>

BAO datasets both for the standard Λ CDM model and multiple extensions to it namely:

- w_0w_a CDM model (M. Chevallier & D. Polarski 2001; E. V. Linder 2003) that includes two more parameters for dark energy namely the equation of state (w_0) and its evolution (w_a);
- a model that includes the sum of neutrino masses $\sum m_\nu \Lambda$ CDM.
- We also explore combinations of the above cosmologies along with the case when the spatial curvature (Ω_k) is also varied in order to study the impact of correlations between the parameters in the extended scenarios.
- Finally, we also show the improvements in constraining power when swapping the SNIa sample from DES-Y5-SNIa to LSST-Y3-SNIa; and the BAO measurements from DESI-DR2-BAO to DESI-DR3-BAO.

Note that in this work we only model SNIa and CMB datasets, and use the covariance matrix for BAO measurements as released by the DESI team. As a result, we do not model any source of systematic uncertainties in the BAO measurements and only use the BAO dataset to assess the expected improvements in cosmological constraints when they are combined with SNIa and CMB data. We also do not attempt to compare the differences between Fisher vs MCMC nor study the choices of binning for BAO measurements.

The paper is organized as follows. In §2, we explain the process to generate mock-data vector and covariance matrices for SNe-Ia, CMB, and BAO datasets along with the noise and foreground modeling for CMB surveys. In §3, we describe the MCMC sampling methods and the Fisher formalism. The results and discussion are given in §4 followed by the conclusion in §5.

2. DATASETS AND EXPERIMENTAL SETUP

In this section, we describe the mock data vectors for SNIa, the CMB power spectra, and BAO, along with a discussion of the corresponding covariance matrices for the three datasets across the experimental surveys considered. We additionally incorporate the original data vectors released by DES-Y5-SNIa and DESI-DR2-BAO for comparison, and we describe these datasets in the corresponding sections below.

2.1. Mock data vectors and baseline cosmological model

We generate the mock data vectors assuming a standard 6-parameter Λ CDM model as the baseline model

based on *Planck* 2018 measurements (TT, TE, EE + lowE + lensing in Table 2 of Planck Collaboration et al. 2020b). The data vectors include the appropriate distance measurements for SNIa and BAO, and also CMB power spectra measurements. These data vectors are discussed in more detail in the subsequent sections. To generate CMB power spectra, we use the Code for Anisotropies in the Microwave Background (CAMB, A. Lewis et al. 2000) software. In Table 1, we list the fiducial values of all the parameters used in this work. We also provide the values used for extended cosmology scenarios that include dark energy and sum of neutrino masses assuming a normal ordering with a fiducial value set to $\sum m_\nu = 0.06\text{eV}$ based on the lower limits from the neutrino oscillation experiments. We also assess the impact of allowing the spatial curvature to vary when considering the above extensions, although we do not focus exclusively on the resulting constraints on spatial curvature in this work. When using SNIa data alone, we restrict the analysis to Λ CDM and w_0w_a CDM cases since SNIa data does not constraint $\sum m_\nu$. The table also lists the priors used for MCMC formalism discussed in §3.1. Besides the fiducial cosmology discussed here, in Appendix B we briefly examine how the constraining power depends on the assumed cosmology by regenerating the constraints for the DES-Y5-SNIa (DES Collaboration et al. 2024a) and DES-Dovekie (B. Popovic et al. 2025) cosmologies.

2.2. LSST-Y3-SNIa data

In this work, we use the mock SNIa catalog from the first three years of LSST data (LSST-Y3-SNIa) generated in A. Mitra et al. (2023) and we refer the reader to that work for more details. Here, we briefly summarize the steps to obtain the mock SNIa catalog. The simulations used for generating the mock catalog are based on the time domain pipeline using PLAsTiCC data (R. Kessler et al. 2019; R. Hložek et al. 2020) that were originally designed for the Rubin LSST-DESC. The mock-data generation can be decomposed into three main stages: (a) standardizing the SNe brightness with the light-curve fitting using SALT2 (J. Guy et al. 2007); (b) generating simulations necessary for Bayesian Estimation Applied to Multiple Species (BEAMS) with Bias Corrections (BBC, R. Kessler & D. Scolnic 2017); and finally (c) constructing the bias-corrected Hubble diagram data along with the statistical and systematic covariance matrices. The simulations adopt standard flat Λ CDM cosmology using the fiducial values listed in Table 1. The noise model for the simulated magnitudes includes contributions from photon noise, calibration errors, and uncertainties in the properties of host-galaxies

Table 1. Fiducial values of the parameters and the associated priors used in this work (Planck Collaboration et al. 2020b). The priors are either flat in the range $\mathcal{U}[\text{min}, \text{max}]$ or Gaussian, $\mathcal{N}(\mu, \sigma^2)$, with widths σ centered at the mean μ . The last column marks the dataset that are sensitive to the parameter under consideration.

Parameter	Fiducial	Prior	Constraining dataset
<i>Cosmological parameters (ΛCDM):</i>			
Amplitude of scalar fluctuations $\ln(10^{10} A_s)$	3.044	$\mathcal{U}[1.6, 3.9]$	CMB, BAO
Dark matter density $\Omega_c h^2$	0.1200	$\mathcal{U}[0.001, 0.99]$	CMB, SNIa, BAO
Baryon density $\Omega_b h^2$	0.02237	$\mathcal{U}[0.005, 0.1]$	CMB, BAO
Scalar spectral index n_s	0.9649	$\mathcal{U}[0.8, 1.2]$	
Hubble parameter h	0.6732	$\mathcal{U}[0.4, 1]$	
Reionization optical depth τ_{re}	0.0544	$\mathcal{N}(0.0544, 0.007^2)$	CMB
<i>Extensions:</i>			
Sum of neutrino masses $\sum m_\nu$ (Normal hierarchy)	0.06 [eV]	$\mathcal{U}[0, 0.5]$	CMB, BAO
Equation of state (EoS) of dark energy w_0	-1	$\mathcal{U}[-10, 10]$	CMB, SNIa, BAO
Time varying dark energy EoS w_a	0	$\mathcal{U}[-30, 20]$	
Spatial curvature Ω_k	0	$\mathcal{U}[-0.3, 0.3]$	CMB, BAO
<i>Nuisance parameters:</i>			
SNIa absolute magnitude \mathcal{M}	-19.5	$\mathcal{U}[-15, -25]$	SNIa
CMB temperature calibration [†] T_{cal}^ν	1	$\mathcal{N}(1, 0.01^2)$	CMB
CMB polarization calibration [†] P_{cal}^ν	1	$\mathcal{N}(1, 0.01^2)$	CMB

NOTE—† - The total number of parameters depends on the number of frequency bands in the CMB experiment. The calibration factors are applied to the theory spectra during the sampling step as described by Eq.(2). The priors are chosen based on some of the recent works in the literature (L. Balkenhol et al. 2021; T. Louis et al. 2025; E. Camphuis et al. 2025).

of SNIa, as well as an empirically determined signal-to-noise (S/N) ratio.

The mock SNIa catalog contains objects whose host-galaxy redshifts z are available either from spectroscopy or from photometry; we refer to these subsamples as z_{spec} and z_{phot} , respectively (A. Mitra et al. 2023). Note that these labels refer solely to how the redshift is obtained, not to how the supernova type is determined. The z_{phot} sample, as expected, is significantly ($\sim 60\%$) larger than the z_{spec} subset, and uses the photometric redshift estimate of the host-galaxy as a prior, adapted from R. Kessler et al. (2010), during the light curve fitting process. The z_{phot} sample makes up most of high redshift $z > 0.08$ objects in the catalog although a minor fraction of spectroscopic events found in the PLAsTiCC subset are also present in the $z > 0.08$ sample. The objects at low- z ($z \leq 0.08$) come from the spectroscopic sample, predicted to be observed by the 4MOST spec-

trograph (C. Frohmaier et al. 2025) with an expected redshift precision of $\sigma_z \sim 10^{-5}$. The low- z z_{spec} sample is simulated using the Data Challenge-2 (DC2, B. O. Sánchez et al. 2022) with a cadence corresponding to the Wide Fast Deep (WFD²) observations; and the high- z simulation is based on the cadence of observations for the Deep Drilling Fields (DDF³). The details of the simulation can be found in §III of A. Mitra et al. (2023).

In total, the LSST-Y3-SNIa dataset used in this analysis contains 5784 SNIa (3551 are photometric and 2233 are spectroscopic objects). We present the redshift distribution and the errors on the distance modulus as a function of redshift in red on the left and right panels of Fig. 1. The errors include both the statistical and

² <https://survey-strategy.lsst.io/baseline/wfd.html>

³ <https://survey-strategy.lsst.io/baseline/ddf.html>

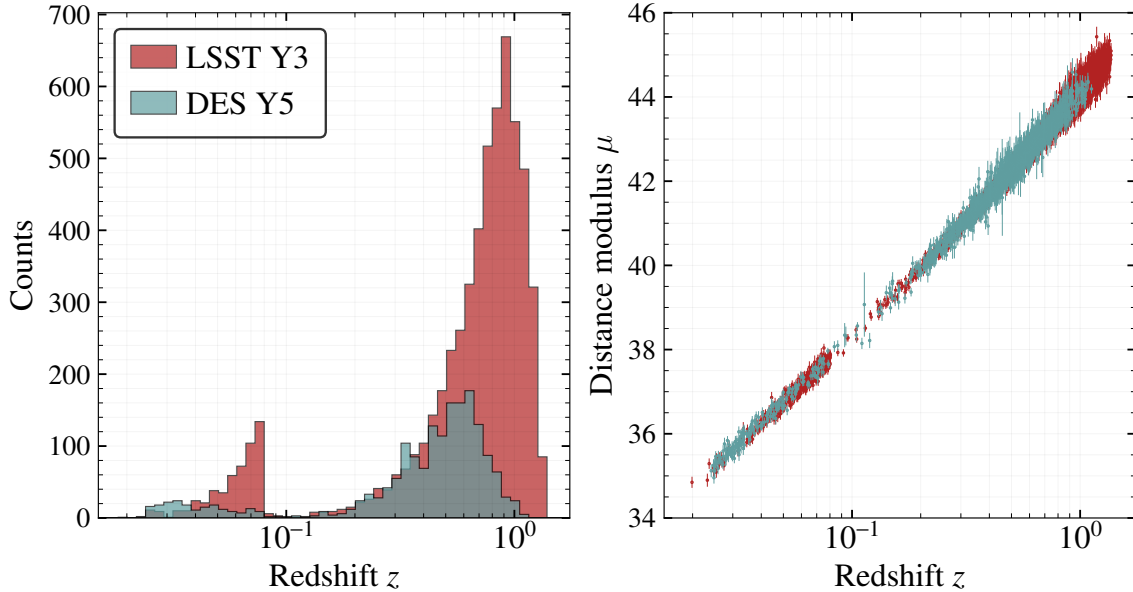


Figure 1. Redshift distribution (left) and the distance modulus as a function of redshift (right) are presented for SNIa samples used in this work. Red distribution represents the LSST-Y3-SNIa mock dataset and we have also shown DES-Y5-SNIa in teal for comparison. The sample size of LSST-Y3-SNIa is roughly $\times 3.3$ larger than DES-Y5-SNIa.

systematic contributions. The LSST-Y3-SNIa consists of ~ 1200 (20%) of the objects at $z \geq 1$.

In the past, analyses using the BBC approach have relied on redshift-binned SNIa samples for cosmological inference to reduce computation time, anticipating much larger datasets in the future (B. Popovic et al. 2021, for example). However, D. Brout et al. (2021) showed that although the statistical covariance of a binned sample can be tuned to match that of an unbinned sample, binning generally leads to larger systematic errors. A subsequent study by R. Kessler et al. (2023) introduced a rebinning scheme based on redshift, stretch, and color, and demonstrated through simulations that this approach reduces systematic errors relative to redshift-only binning. Nevertheless, a fully optimal binning strategy capable of reducing uncertainties to the level of the unbinned case is yet to be established. Subsequently, other recent works (M. Vincenzi et al. 2024; DES Collaboration et al. 2024a; B. Popovic et al. 2025) have worked with the unbinned sample for cosmological inference. Besides the fiducial unbinned LSST-Y3-SNIa sample, we also forecast cosmological constraints using an alternative LSST-Y3-SNIa sample binned following R. Kessler et al. (2023) into 14 redshift bins.

Comparison with DES-Y5-SNIa: Beyond LSST-Y3-SNIa, which constitutes the baseline SNIa sample in this analysis, we additionally employ the DES-Y5-SNIa sample (M. Vincenzi et al. 2024; DES Collabo-

ration et al. 2024a; B. Popovic et al. 2021) for comparison. For this dataset, we use both the original DES-Y5-SNIa data vector and a mock data vector generated using the same prescription applied to the LSST-Y3-SNIa sample described above. The covariance matrix is adopted directly from the original DES-Y5-SNIa release. The LSST-Y3-SNIa SNIa sample is $\times 3.3$ larger than the DES-Y5-SNIa SNIa, which is also shown in the Fig. 1 in teal for comparison. The DES-Y5-SNIa consists of 1754 objects after removing the false positives (1829 in total) in the range $z \in [0.025, 1.12]$. The mean redshift \bar{z} of the DES-Y5-SNIa sample is $\bar{z} = 0.46$ while for the LSST-Y3-SNIa, it is $\bar{z} = 0.72$.

2.3. CMB data

We consider three different experiments for CMB data: the ongoing South Pole Telescope (SPT-3G) survey (B. A. Benson et al. 2014; A. N. Bender et al. 2018; K. Prabhu et al. 2024; A. Vitriier et al. 2025); ASO (The Simons Observatory Collaboration et al. 2025); and a future CMB survey matching the specifications of the CMB-S4 survey (CMB-S4 Collaboration 2019) which we represent as $\overline{\text{CMB}} - \text{S4}$. The observables for CMB are the temperature, polarization, and lensing power spectra $TT, EE, TE, \phi\phi$.

SPT-3G: For SPT-3G, we consider the Ext-10k survey described in K. Prabhu et al. (2024); A. Vitriier et al. (2025) that covers $f_{\text{sky}} = 0.25$ ($10,000 \text{ deg}^2$) of the southern sky excluding regions contaminated by the

Table 2. Experimental beam, sky fraction, and noise levels for different surveys considered in this work. For polarization noise, we use $\Delta_P = \sqrt{2}\Delta_T \mu\text{K arcmin}$.

Survey	Sky fraction f_{sky}	Beam θ_{FWHM} in arcminutes (Noise Δ_T in $\mu\text{K arcmin}$)					
		30 GHz	40 GHz	90 GHz	150 GHz	220 GHz	280 GHz
SPT-3G Main	0.036			1.7 (2.5)	1.2 (2.1)	1 (7.6)	
SPT-3G Summer	0.065	-	-	1.7 (9.4)	1.2 (8.7)	1 (29.5)	-
SPT-3G Wide	0.145			1.7 (14)	1.2 (12)	1 (42)	
ASO-Baseline	0.4	7.4 (61)	5.1 (30)	2.2 (5.3)	1.4 (6.6)	1 (15)	0.9 (35)
ASO-Goal		7.4 (44)	5.1 (23)	2.2 (3.8)	1.4 (4.1)	1 (10)	0.9 (25)
$\overline{\text{CMB}} - \overline{\text{S4}}$	0.57	7.8 (27.1)	5.3 (11.6)	2.2 (2)	1.4 (2)	1 (6.9)	0.9 (16.7)

Table 3. Atmospheric noise specifications for TT/EE power spectra measurements from SPT and $\overline{\text{CMB}} - \overline{\text{S4}}$ surveys. Atmospheric noise is uncorrelated between CMB temperature and polarization, and hence TE is assumed to be zero. The values for SPT are derived from actual observations (K. Prabhu et al. 2024) and for $\overline{\text{CMB}} - \overline{\text{S4}}$, the values are obtained from CMB-S4 Collaboration (2019). For ASO, we use the publicly available noise calculator (https://github.com/simonsobs/so_noise_models) as mentioned in the text.

Survey	$\ell_{\text{knee}}, \alpha_{\text{knee}}$					
	30 GHz	40 GHz	90 GHz	150 GHz	220 GHz	280 GHz
<i>CMB temperature TT spectra:</i>						
SPT-3G Main			1200, -3	2200, -4	2300, -3	
SPT-3G Summer	-	-	1600, -4.5	2600, -4	2600, -3.9	-
SPT-3G Wide						
$\overline{\text{CMB}} - \overline{\text{S4}}$	1200, 4.2	1200, 4.2	1200, 4.2	1900, 4.1	2100, 4.1	2100, 3.9
<i>CMB polarization EE spectra:</i>						
SPT-3G Main			300, -1	300, -1	300, -1	
SPT-3G Summer	-	-	300, -2.2	490, -2	500, -2.5	-
SPT-3G Wide						
$\overline{\text{CMB}} - \overline{\text{S4}}$	150, 2.7	150, 2.7	150, 2.6	220, 2.2	200, 2.2	200, 2.2

galactic foregrounds. This Ext-10k survey is composed of three different surveys with different noise properties and sky fractions: (a) the deep SPT-3G Main field comprising of $f_{\text{sky}} = 0.036$ (1500 deg^2); (b) the summer fields covering roughly $f_{\text{sky}} = 0.065$ (2650 deg^2); and (c) the wide fields with a sky fraction of roughly $f_{\text{sky}} = 0.145$ (6000 deg^2).

ASO: For ASO, we perform forecasts for two configurations: ASO-Baseline and ASO-Goal (The Simons Observatory Collaboration et al. 2025). For both these configurations, we assume a sky fraction of $f_{\text{sky}} = 0.4$, which is roughly $16,500 \text{ deg}^2$ after excluding the regions contaminated by the galactic foregrounds (The Simons

Observatory Collaboration et al. 2018, 2025).

$\overline{\text{CMB}} - \overline{\text{S4}}$: For $\overline{\text{CMB}} - \overline{\text{S4}}$, we only consider a wide-area survey expected to be carried out in Chile similar to the one originally planned by the CMB-S4 experiment with $f_{\text{sky}} = 0.67$ (CMB-S4 Collaboration 2019). We remove the regions with high levels of galactic foreground emission, using *Planck*'s GAL090 mask and assume a remaining sky fraction of $f_{\text{sky}} = 0.57$ (CMB-S4 Collaboration 2019) for the subsequent calculations here.

2.3.1. Noise and foreground modeling

For all the above experiments, we use data from the multiple frequency bands. The noise in the individual bands receives contribution from the detector white

noise and atmospheric noise, and the noise power spectrum is modeled as

$$N_\ell^{XX} = \Delta_X^2 \left[1 + \left(\frac{\ell}{\ell_{\text{knee}}} \right)^{\alpha_{\text{knee}}} \right], \quad (1)$$

where Δ_X corresponds to the white noise levels in the temperature (T) and polarization (P) maps; and $(\ell_{\text{knee}}, \alpha_{\text{knee}})$ are used to model the contribution from the atmospheric noise. In Table 2, we list the values used for noise along with the experimental beam and sky fractions. In Table 3, we give the values used for atmospheric noise modeling for SPT-3G and CMB-S4. These are based on CMB-S4 Collaboration (2019); S. Raghunathan & Y. Omori (2023); K. Prabhu et al. (2024). For ASO, we use the publicly available noise model downloaded from this link⁴.

Since the CMB maps receive contributions from extragalactic foreground signals we also include them in our analysis. They can be decomposed into contributions from radio and dusty star-forming galaxies, as well as the kinematic and thermal Sunyaev–Zeldovich (kSZ and tSZ) effects. These signals are modeled using measurements from the SPT (C. L. Reichardt et al. 2021). In the modeling scheme, we have ignored the contribution from bright point sources with flux $S_{150} \geq 3\text{mJy}$ at 150 GHz and also clusters detected above a signal-to-noise $S/N \geq 5$ for all the experiments (S. Raghunathan 2022). We refer the reader to S. Raghunathan & Y. Omori (2023) for details about the details on modeling the temperature portion of the extragalactic foreground signals. For polarization, we assume a 3% polarization fraction for radio and dusty galaxies based on R. Datta et al. (2018); N. Gupta et al. (2019) but ignore the polarized SZ contributions.

We do not include the galactic foreground signals, since we are already applying a conservative cut in our sky fraction to remove the contaminated regions (See Table 2). In the unmasked region, the galactic foregrounds are expected to be subdominant, and including them has a negligible effect on the cosmological constraints (K. Prabhu et al. 2024). Nevertheless, we introduce a conservative scale cut $\ell_{\text{min}} = 300$ to remove large-scale modes where the contribution from the galactic foreground signals could be generally significant.

2.4. Binning, multipole ranges, lensing noise and covariance matrix

The information from all the bands are optimally combined, using internal linear combination (ILC) technique, to reduce the overall variance from noise and

foreground signals (J.-F. Cardoso et al. 2008; S. Raghunathan & Y. Omori 2023).

During the ILC step, we also take the frequency-dependent temperature T_{cal}^ν and polarization P_{cal}^ν calibration factors into account. The calibration factors are obtained by cross-correlating the CMB maps from a given survey with *Planck* maps and defined as $X_{\text{cal}}^{\text{survey}} = \sqrt{C_\ell^{\text{survey} \times \text{Planck}} / C_\ell^{\text{Planck}_1 \times \text{Planck}_2}}$ with $X \in [T, P]$ (E. Camphuis et al. 2025, for example). The subscripts *Planck*₁ and *Planck*₂ indicate the two *Planck* datasets with mutually uncorrelated noise to avoid the noise bias in the denominator. The calibration is performed separately for each frequency band, either by cross-correlating with the corresponding *Planck* band or by determining a calibration factor for a single band (typically 150 GHz) using the *Planck* cross-correlation, after which the remaining bands are calibrated internally. As we will see below in §3, we allow the calibration parameters to vary during the fitting process and marginalize over them to obtain cosmological constraints. The calibration factors are applied to the theory spectra $C_\ell^{TT}, C_\ell^{EE}, C_\ell^{TE}$ as:

$$\begin{aligned} C_\ell^{TT, \nu_1 \nu_2} &= \frac{C_\ell^{TT, \nu_1 \nu_2}}{T_{\text{cal}}^{\nu_1} T_{\text{cal}}^{\nu_2}}, \\ C_\ell^{EE, \nu_1 \nu_2} &= \frac{C_\ell^{EE, \nu_1 \nu_2}}{P_{\text{cal}}^{\nu_1} P_{\text{cal}}^{\nu_2}}, \\ C_\ell^{TE, \nu_1 \nu_2} &= \frac{2C_\ell^{TE, \nu_1 \nu_2}}{T_{\text{cal}}^{\nu_1} P_{\text{cal}}^{\nu_2} + T_{\text{cal}}^{\nu_2} P_{\text{cal}}^{\nu_1}} \end{aligned} \quad (2)$$

The ILC technique is equivalent to the inverse variance combination of data from all the bands but after taking into account the correlation between different frequency bands, caused by foreground signals, into account. In the absence of correlation between frequency bands, this simplifies to $N_\ell^{\text{ILC}} = \sum_i \frac{1}{N_\ell^{\nu_i}}$. The ILC residuals N_ℓ^{ILC} contain residual signals from both noise and foregrounds components.

We combine the ILC residuals with the signal power spectra $C_\ell^{TT} / C_\ell^{EE} / C_\ell^{TE}$ to compute the covariance matrix, as described below. To obtain the final observed power spectra (the data vector) for different experiments, we use only the signal power spectra. Consequently, we do not marginalize over any foreground parameters. We note that this choice may lead to slightly optimistic constraints for CMB TT -only spectra, but it should have a negligible impact once $EE/TE/\phi\phi$ measurements and other external datasets are included. The spectra are binned with $\Delta_\ell = 100$ with uniform weights for all multipoles in a conservative ℓ range $[\ell_{\text{min}}, \ell_{\text{max}}] = [300, 3500]$ for all the experiments. We compare and quantify the constraining power with different binning schemes in §4.3.

⁴ https://github.com/simonsobs/so_noise_models

We adopt the same ranges for lensing reconstruction using the standard lensing quadratic estimator (W. Hu & T. Okamoto 2002; T. Okamoto & W. Hu 2003) and compute the lensing noise. The lensing noise spectrum can be decomposed into $N_L^{\phi\phi} = N_L^{(0,\phi\phi)} + N_L^{(1,\phi\phi)} + N_L^{(3/2,\phi\phi)} + \dots \equiv N_L^{(0,\phi\phi)}$ (M. S. Madhavacheril et al. 2020). While the higher order biases are important to obtain an unbiased lensing power spectrum, particularly for the current and future low-noise CMB datasets, they are much smaller ($\lesssim 2\%$) compared to $N_L^{(0,\phi\phi)}$ which dominates the error budget. Subsequently, we only consider $N_L^{(0,\phi\phi)}$ as the source of lensing noise. The sQE is known to be sensitive to the contamination from the non-Gaussian astrophysical foregrounds on small-scales (M. S. Madhavacheril & J. C. Hill 2018; S. Ferraro & J. C. Hill 2018), and several modified lensing estimators have been introduced to robustly reconstruct lensing at the expense of increased statistical errors (T. Namikawa et al. 2013; S. J. Osborne et al. 2014; M. S. Madhavacheril & J. C. Hill 2018; E. Schaan & S. Ferraro 2019; N. Sailer et al. 2023; S. Raghunathan & Y. Omori 2023). In this work, we do not use these modified lensing estimators but employ a stringent cut on the maximum multipole $\ell = 3500$

used for lensing reconstruction to mitigate the contamination from foreground signals. We note that this choice of $\ell_{\max} = 3500$ is conservative for polarization channels since the extragalactic foregrounds are largely unpolarized (N. Gupta et al. 2019; R. Datta et al. 2018). Similar to the CMB power spectra, we bin the lensing power spectrum $C_L^{\phi\phi} = C_{L,\text{signal}}^{\phi\phi} + N_L^{\phi\phi}$ with $\Delta_L = 100$ in the range $[L_{\min}, L_{\max}] = [30, 3500]$. Note that we use the subscript L to represent the modes of the lensing power spectrum rather than the ℓ that is used for $TT/EE/TE$ spectra. This is to differentiate between the reconstructed lensing information using the lensing-induced correlation between two Fourier modes ℓ and ℓ' with $L = \ell - \ell'$ (F. Bernardeau 1997; T. Okamoto & W. Hu 2003). This also let us reconstruct the largest scale modes and hence we set $L_{\min} = 30$ for the lensing power spectrum.

The covariance matrix $\Sigma_{\ell,\ell'}$ has the length $N_{\text{bins}} \times N_{\text{obs}}$ on each side with the total number of multipole bins $N_{\text{bins}} = \sum_{XX} N_{\text{bins}}^{XX}$ and N_{obs} corresponds to the total number of power spectra $XX \in [TT, EE, TE, \phi\phi]$. The diagonal blocks of the covariance matrix at each multipole ℓ is given as

$$\Sigma_{\ell,\ell}^{XY} = \frac{2}{(2\ell + 1) f_{\text{sky}}} \begin{pmatrix} (\tilde{C}_\ell^{TT})^2 & (C_\ell^{TE})^2 & \tilde{C}_\ell^{TT} C_\ell^{TE} & 0 \\ (C_\ell^{TE})^2 & (\tilde{C}_\ell^{EE})^2 & \tilde{C}_\ell^{EE} C_\ell^{TE} & 0 \\ \tilde{C}_\ell^{TT} C_\ell^{TE} & \tilde{C}_\ell^{EE} C_\ell^{TE} & \frac{[(C_\ell^{TE})^2 + \tilde{C}_\ell^{TT} \tilde{C}_\ell^{EE}]}{2} & 0 \\ 0 & 0 & 0 & (\tilde{C}_L^{\phi\phi})^2 \end{pmatrix}. \quad (3)$$

where C_ℓ^{XX} and $C_L^{\phi\phi}$ corresponds to the lensed CMB and CMB-lensing power spectra. We set the off-diagonal blocks, representing correlation between adjacent multipole bins, $\Sigma_{\ell,\ell'}^{XY} = 0$. While there exists a non-zero correlation between lensed CMB and CMB-lensing spectra, they are expected to be small and hence we ignore them (C. Trendafilova 2023). We note that the exclusion of this term can result in slightly ($\sim 10\%$) optimistic parameter constraints but it has been found to have negligible impact when external datasets, as is the case in this work, are included (J. Peloton et al. 2017). In Eq.(3), f_{sky} is the sky fraction of the CMB survey given in Table 2. The fields with the tilde symbol represent the combination of signal and noise spectra as

$$\tilde{C}_\ell^{XX} = C_\ell^{XX} + N_\ell^{\text{ILC},XX}, \quad (4)$$

$$\tilde{C}_L^{\phi\phi} = C_L^{\phi\phi} + N_L^{(0,\phi\phi)}. \quad (5)$$

where signal spectra correspond to $XX \in [TT, EE]$ and the noise spectra $N_\ell^{\text{ILC},TT}$ and $N_\ell^{\text{ILC},EE}$ are the residual noise and extragalactic foreground signals after the ILC step. Note that we do not represent C_ℓ^{TE} with the tilde since (a) the noise is uncorrelated between the CMB temperature and polarization maps, (b) we are ignoring the impact of galactic foregrounds, and (c) the polarization fraction of the foreground signals has been found to be negligible (R. Datta et al. 2018; N. Gupta et al. 2019). Including the small TE correlation due to the non-zero (3%) polarization fraction assumed for extragalactic sources has no impact on our final results.

2.5. BAO data

For the BAO measurements, we use the recently released DESI DR2 measurements (Table IV of DESI Collaboration et al. 2025) and also the forecast for the up-

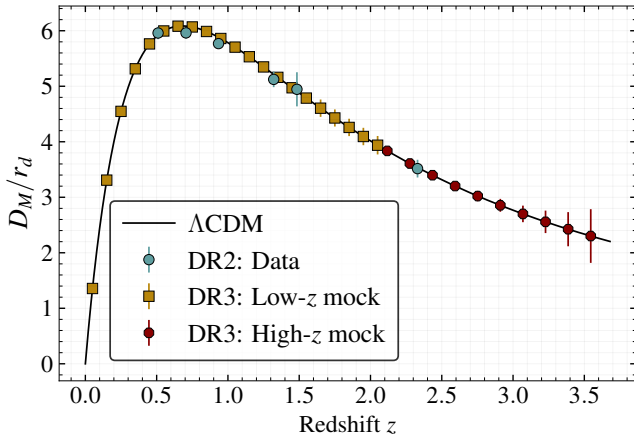


Figure 2. Distance measurements D_M/r_d from DESI DR2 release (teal circles, DESI Collaboration et al. 2025) along with the expectations from the next DR3 release. For DR3, we show the low- (high-redshift) measurements from the clustering of galaxies and quasars (Ly- α forest) at $z \lesssim 2$ ($z > 2$) in yellow squares (red hexagons). The DR2 values are actual measurements while the DR3 values are expectations from Λ CDM (black curve) along with the forecasted errors.

coming DR3 release (DESI Collaboration 2023) which aims to extend the measurements to significantly higher redshifts ($z_{\max}^{\text{DR3}} = 3.55$) compared to DR2 ($z_{\max}^{\text{DR2}} = 2.05$). The forecasted data vectors are based on clustering of galaxies and quasars at low redshifts $z \lesssim 2$ and the clustering of Ly- α forest at higher redshifts $z \geq 2$ identified from the spectra of quasars.

The main observables measured by BAO are the distance ratio $D_H(z)/r_d = \frac{c}{H(z)r_d}$ and $D_M(z)/r_d$ (DESI Collaboration et al. 2025) where $H(z)$ is the Hubble function; and D_H and D_M are the Hubble and comoving transverse distances (D. W. Hogg 1999), both expressed in terms of the scale of the sound horizon r_d in Mpc. If the galaxy clustering measurement shape is fully interpreted, it gives a redshift space distortion measurement of $f\sigma_8(z)$ ⁵ which is the product of the growth rate f and the amplitude of matter density fluctuations at $8h^{-1}$ Mpc scale σ_8 . At any given redshift, there are significant correlations between all the above observables, and these are taken into account in our analysis using the covariance matrix (see Table IV of DESI Collaboration et al. 2025, for example).

In Fig. 2, we show the actual measurements D_M/r_d from DESI DR2 release as teal circles along with the forecasts matching the specifications for the upcoming DESI DR3 release. For DR3, the yellow squares corre-

spond to the low redshift clustering from galaxies and quasars, and the red hexagons correspond to the measurements of the clustering of Ly- α forest at high redshifts. As it is evident from Fig. 2, the DR3 release has a lot more high redshift Ly- α measurements compared to DR2 and these have the potential to significantly improve the cosmological constraints as we will see below. For the forecasting purposes, we use the covariance matrix released by the DESI collaboration, without any scaling, but create our own data vectors both for the DR2 and DR3 datasets assuming the fiducial cosmology (Planck Collaboration et al. 2020a) to match the the analysis choices of CMB and SNe datasets. The black curve in Fig. 2 shows the Λ CDM expectation.

For reference, we list the forecasted data vectors used in this work in Appendix C. The forecasted data vectors for DESI-DR2-BAO are in Table C1 with the covariance being the same as listed in Table 1 of DESI Collaboration et al. (2025). For DESI-DR3-BAO, the data vectors are decomposed into low and high redshift measurements, and are listed in Table C3 and Table C2. Besides the data vectors, the tables also contain the correlations between observables A and B as $\rho(A, B)$ where $A, B \in [H_z/r_d, D_A/r_d, f\sigma_8]$.

3. METHODOLOGY

3.1. MCMC

We use the Code for BAYesian Analysis (cobaya⁶, J. Torrado & A. Lewis 2019) to sample the posteriors using the Metropolis-Hastings MCMC algorithm. For theory calculations, we make use of the CAMB (A. Lewis et al. 2000) software, the Einstein-Boltzmann solver, which is inbuilt within cobaya. To achieve chain-convergence, we use the Gelman-Rubin statistic $R - 1 = 0.01$, as implemented in (A. Lewis 2013). The chains are analyzed using the GetDist⁷ package. We set the initial 30% of the chains as the burn-in phase and disregard those samples in all cases.

In Table 1, we list the set of cosmological and nuisance parameters that are sampled during the MCMC. The fiducial values and the prior ranges are provided; and we also mark the datasets that are sensitive to the parameter under consideration in the last column. We choose wide priors on w_0 and w_a based on the recent results (see Table 1 of C. L. Steinhardt et al. 2025) where the authors pointed out significant shifts in the inferred values of parameters like $\Omega_c h^2$ based on the chosen prior ranges. We note that this choice of prior al-

⁵ Only forecasted for DESI-DR3-BAO at the moment.

⁶ <https://cobaya.readthedocs.io/en/latest/>

⁷ <https://getdist.readthedocs.io/en/latest/index.html>

lows the phantom-crossing (A. Vikman 2005; S. Nojiri & S. D. Odintsov 2005) with $w_0 < -1$ violating the null energy condition. The $w_0 < -1$ scenario is handled using the parametrized post-Friedmann (PPF) approach in CAMB (W. Fang et al. 2008; R. R. Caldwell & E. V. Linder 2025). The likelihood code is publicly available for downloading through this link⁸.

3.2. Fisher formalism

Besides the MCMC approach, we also compute the parameter constraints using the standard Fisher formalism, in order to compare the constraints from both the methods. As mentioned earlier, this test is limited to CMB and SNIa datasets only. We build the Fisher matrices as described below.

3.2.1. Fisher matrix for CMB power spectra

For CMB, we use the lensed CMB power spectra of the temperature and polarization fields, and form the Fisher matrix as (G. Jungman et al. 1996; M. Tegmark et al. 1997; S. Galli et al. 2014)

$$\mathcal{F}_{\alpha\beta}^{\text{CMB}} = \sum_{XX,YY} \sum_{\ell=\ell_{\min}}^{\ell_{\max}} \frac{\partial C_{\ell}^{XX}}{\partial \theta_{\alpha}} \cdot (\Sigma_{\ell,\ell}^{XY})^{-1} \cdot \frac{\partial C_{\ell}^{YY}}{\partial \theta_{\beta}}, \quad (6)$$

where $XX, YY \in [TT/EE/TE]$ power spectra with $(\ell_{\min}, \ell_{\max}) = (300, 3500)$; θ_{α} represents the parameters being constrained; $\partial C_{\ell}/\partial \theta_{\alpha}$ is the partial derivatives of the lensed CMB spectra with respect to the parameters θ and the derivatives are obtained using the finite difference method; and $\Sigma_{\ell,\ell}$ is the covariance matrix of the lensed CMB power spectra (without including the CMB-lensing spectrum in this case) as given in Eq.(3).

3.2.2. Fisher matrix for SNIa

For SNIa, we construct the Fisher matrix as,

$$\mathcal{F}_{\alpha\beta}^{\text{SNIa}} = \sum_{ij} \frac{\partial \mu_i}{\partial \theta_{\alpha}} \cdot \Sigma_{ij}^{-1} \cdot \frac{\partial \mu_j}{\partial \theta_{\beta}}, \quad (7)$$

where μ represents the distance modulus of the i^{th} SNIa at redshift z_i , $\frac{\partial \mu}{\partial \theta}$ is the partial derivative of the distance modulus with respect to parameter θ calculated using finite difference method, and the summation runs over all the SNIa in catalog. In Eq.(7), the covariance matrix Σ_{ij} is the combination of statistical and systematic covariance matrix. The presence of systematic errors introduces correlation between different SNIa and hence

Σ_{ij} is a non-diagonal matrix. In the absence of systematic errors, though, Eq.(7) reduces to

$$\mathcal{F}_{\alpha\beta}^{\text{SNIa}} = \sum_i \frac{\partial \mu_i}{\partial \theta_{\alpha}} \cdot \frac{1}{\sigma_{\mu_i}^2} \cdot \frac{\partial \mu_i}{\partial \theta_{\beta}}. \quad (8)$$

Details about the statistical and systematic errors for SNIa data are described in §2.2.

4. RESULTS AND DISCUSSION

We start with the comparison of constraints (a) between the recently released DES-Y5-SNIa and LSST SNIa sample, and similarly (b) when swapping the BAO measurements from DESI-DR2-BAO to DESI-DR3-BAO. These are followed by a comparison of the results from the MCMC and Fisher analyses, as well as an examination of the degradation of constraints due to binning, both of which are restricted to the CMB and SNIa datasets. Next, we present constraints on Λ CDM and the extensions, from CMB, SNIa, and BAO, both individually and jointly. As a reminder, all results apart from the comparisons presented in §4.3 are derived from the MCMC analysis.

4.1. Expected improvement from LSST-Y3-SNIa compared to DES-Y5-SNIa

To compare the constraints from DES-Y5-SNIa and the ones expected from LSST-Y3-SNIa, we consider two cosmologies: (A) standard Λ CDM, and (B) $w_0 w_a$ CDM. We present the results for the latter in Fig. 3. For this test, we do not use the official DES chains; instead, we run our own chains. As mentioned earlier, we run chains both using the original DES-Y5-SNIa and the mock data vector generated in this work. In the figure, red contours correspond to LSST-Y3-SNIa and the solid (dash-dotted) teal contours are for DES-Y5-SNIa mock (original data). The dash-dotted teal contours agree (See Fig. 8 of DES Collaboration et al. 2024a) well with the original results (DES Collaboration et al. 2024b; M. Vincenzi et al. 2024; C. L. Steinhardt et al. 2025).

For case (A), we only allow the physical matter density $\Omega_c h^2$ (but the value of H_0 is fixed) and the absolute magnitude nuisance-parameter to vary with the rest of the parameter values fixed using *Planck* Λ CDM values as described in Table 1. In this case, we obtain $\Omega_m = 0.316 \pm 0.013$ for DES-Y5-SNIa mock and $\Omega_m = 0.3152 \pm 0.0048$ for LSST-Y3-SNIa, indicating a $\times 2.7$ improvement in the constraining power.

On the other hand, for case (B), $w_0 w_a$ CDM cosmology, we find that LSST-Y3-SNIa can improve the uncertainties on $\theta \in [w_0, w_a]$ by roughly $\times 2 - \times 2.5$ compared to the DES-Y5-SNIa mock sample. We perform two tests to understand where the improvement comes from when switching to LSST-Y3-SNIa.

⁸ https://github.com/sriniraghunathan/CMB_BAO_SNe_likelihoods

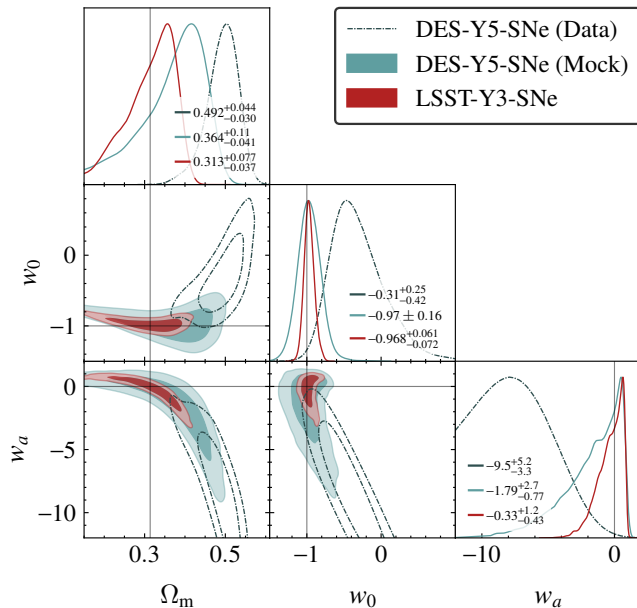


Figure 3. Constraints on dark energy EoS parameters and the matter density: Teal color shows the constraints from DES-Y5-SNIa sample: dash-dotted corresponds to the actual constraints similar to the original works (DES Collaboration et al. 2024a; M. Vincenzi et al. 2024; C. L. Steinhardt et al. 2025) while the solid contours correspond to a mock dataset with DES-Y5-SNIa-like errors, but simulated assuming the fiducial cosmology as specified in Table 1, that is different from the one derived using DES-Y5-SNIa. The expected constraints from LSST-Y3-SNIa are shown in red. We find that the uncertainties on dark energy parameters can be reduced by $\times 2 - \times 2.5$ with LSST-Y3-SNIa relative to DES. The majority of this constraining power comes from the increased number density in the LSST sample compared to DES, with roughly $\times 1.3 - \times 1.5$ contributed by objects at $z \geq 1$.

The first test isolates the contribution from SNe with $z \geq z_{\max}^{\text{DES}}$ by imposing a $z_{\max} > 1$ cut on the LSST-Y3-SNIa, roughly matching the DES redshift range. For this case, we find that the errors on $\sigma(w_0)$ ($\sigma(w_a)$) can be improved by a $\times 1.9$ ($\times 1.6$) by LSST compared to DES. This suggests that ignoring high redshift ($z \geq 1$) SNIa in LSST reduces the constraining power on dark energy parameters by $\sim \times 1.3 - 1.5$. We demonstrate this using yellow contours in Fig. A1.

In the second test, we assess the improvement due to calibration errors in LSST. For this purpose, we select a subset of the LSST-Y3-SNIa with a redshift distribution dN/dz matched to that of the DES sample. We repeat this test five times and find that dark energy constraints to be not significantly different compared to the constraints from DES-Y5-SNIa mock sample. This is shown as red contours in Fig. A1 of the appendix.

These two tests indicate that the majority of the improvement from LSST-Y3-SNIa arises from the increased number density and the inclusion of high-redshift SNIa in the LSST-Y3-SNIa, and not due to changes/improvements in calibration errors. This is also in agreement with the errors shown in Fig. 1, which do not differ significantly between the LSST and DES samples.

As shown in Table 1, we use wide priors for both w_0 and w_a . Restricting them to a narrower range $\mathcal{U}[-3, 1]$ for w_0 and $\mathcal{U}[-3, 3]$ for w_a artificially shifts the inferred values significantly. In this case, we obtain the following values with the original DES-Y5-SNIa SNIa dataset: $\Omega_m = 0.379^{+0.064}_{-0.027}$; $w_0 = -0.82^{+0.14}_{-0.11}$; and $w_a < 0.0520$ (95 % C.L.). These results are similar to the values reported by C. L. Steinhardt et al. (2025), who emphasized the importance of the assumed priors when combining multiple cosmological datasets.

4.2. Expected improvement from DESI-DR3-BAO compared to DESI-DR2-BAO

In this subsection, we present the expected improvement from the upcoming DESI DR3 release (DESI Collaboration 2023) compared to the recent DR2 (DESI Collaboration et al. 2025) dataset. Specifically, we present the constraints for the $r_d H_0 - \Omega_m$ plane, without including any other priors, for the standard Λ CDM cosmology where all the parameters are allowed to vary in the prior range given in Table 1. Note that the BAO measurements need external priors on the scale of the sound horizon since they measure the product of $r_d H_0$.

In Fig. 4, we show the results for DESI-DR2-BAO in teal: dash-dotted curves are for the actual dataset from DESI Collaboration et al. (2025), whereas the corresponding mock-dataset results are shown using solid curves. This can be compared to Figs: 7 and 8 of (DESI Collaboration et al. 2025) and our results agree with the original work. The constraints from the low redshift clustering of galaxies and quasars in the DR3 mock dataset is represented using the open red contour and the ones from the clustering of high redshift Ly- α forest measurements is shown using the open yellow contour. The combined DR3 constraints is shown in orange. The constraints are also listed as a table in the figure for reference. We obtain $\times 1.5$ improvement in the uncertainties for both $r_d H_0$ and Ω_m with the DR3 sample compared to the DR2 release.

The majority of the constraining power comes from the improvement in the low- z sample. On the other hand, the high- z also contributes a little, particularly due to a small change in the direction of degeneracy compared to the low- z sample, as can be seen in the

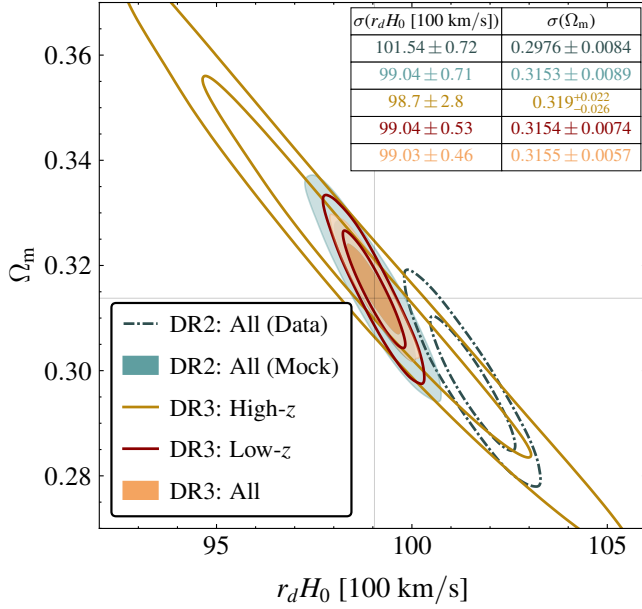


Figure 4. Comparing the constraints in the $r_d H_0 - \Omega_m$ plane for Λ CDM cosmology between DESI DR2 (teal) (DESI Collaboration et al. 2025) and the upcoming DR3 dataset (orange). For DR2, we present constraints derived from the actual DESI DR2 dataset (DESI Collaboration et al. 2025), shown with dash-dotted curves, and from the mock data vectors, drawn with a different cosmology given in Table 1, shown with solid curves. For DR3, we show the constraints for the sample containing BAO measurements from galaxies/quasars at $z \lesssim 2$ in red and the ones from Ly- α forest at $z > 2$ in yellow. We see $\times 1.5$ improvement in the uncertainties on both parameters when switching from DR2 to DR3. While not shown in this figure, the uncertainties in w_0, w_a improve by $\times 1.8$ with DR3 relative to the DR2 measurements. Such improvements will be crucial in addressing the growing tension between CMB and BAO.

figure. While not shown in the figure, for $w_0 w_a$ CDM cosmology, the uncertainties on w_0, w_a reduce by $\times 1.8$ when switching from the DR2 to DR3 sample. Apart from separating the high- z Ly- α forest BAO measurements from the galaxy/quasar measurements at $z \lesssim 2$, we do not investigate alternative BAO binning choices and leave such explorations to future work.

The improvements expected from the DR3 release will be crucial in addressing the tensions between BAO and other observables, like the CMB, that is starting to grow as pointed out recently by many works (E. Camphuis et al. 2025; E. G. M. Ferreira et al. 2025; D. D. Y. Ong et al. 2026, for example). Furthermore, given the improvements in the high redshift measurements, comparing constraints from low- z and high- z (not necessarily as defined in this work) can provide useful systematic checks since the non-linearities in structure formation

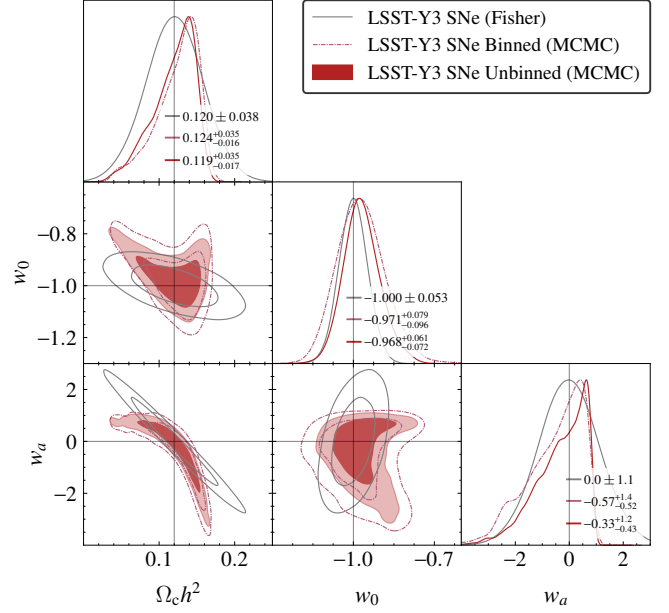


Figure 5. Comparison of the constraints derived using the Fisher formalism in open gray contours and MCMC in red for the LSST-Y3-SNIa. For MCMC, we present the results for both the unbinned (filled contours) and binned (open contours). The filled red contours are the same as in Fig. 3. The posteriors are significantly non-Gaussian which are not captured by the Fisher formalism. We find that binning the SNIa sample reduces the constraining power by $\sim 30\%$ for the dark energy parameters.

can be more important for the low- z sample compared to the high- z .

4.3. Comparison of Fisher-forecast and MCMC-derived constraints, and the impact of binning for both SNIa and CMB

SNIa: For SNe, we compare the results from LSST-Y3-SNIa for $w_0 w_a$ CDM cosmology and they are presented in Fig. 5. Since the SNIa distance modulus measurements are most sensitive to only a subset of cosmological parameters $\theta \in [\Omega_c h^2, w_0, w_a]$, we only compare the constraints for these ones. The fiducial values for the other parameters are to the values indicated in Table 1. The Fisher constraints are shown as open gray contours and the equivalent constraints from MCMC are in red: solid is for the unbinned sample (same as Fig. 3) and dash-dotted is for the binned sample. As evident from the figure, the posteriors are strongly non-Gaussian, a feature that the Fisher formalism cannot capture. Due to the non-Gaussian nature of the posterior distribution and strong parameter degeneracies, projection effects appear in the MCMC results, as indicated by the red contours. This, however, does not introduce significant shifts in the inferred values. As discussed later

in §4.4, once the SNIa sample is combined with BAO and/or CMB, the posteriors become sufficiently Gaussian compared to the SNIa-only case.

In the figure, we also show the MCMC results obtained using the binned SNIa sample as open red contours. As a reminder, for the binned case, the 5800 SNIa in the LSST-Y3-SNIa are binned based on the rebinning approach in R. Kessler et al. (2023) into 14 redshift bins. For w_0w_a CDM cosmology, we find that the binned case degrades the uncertainties on w_0, w_a by $\sim \times 1.3$ compared to the unbinned case. In the case of Λ CDM cosmology (not shown in Fig. 3), when only the matter density Ω_m parameter is allowed to vary, we get $\Omega_m = 0.3152 \pm 0.0048$ (0.3154 ± 0.0069) for the unbinned (binned) analysis, corresponding to a slightly higher degradation than for the w_0w_a CDM case.

CMB: In Fig. 6, we compare the Λ CDM constraints obtained using the $TT/EE/TE$ power spectra measurements expected from CMB – S4, the most constraining CMB dataset in this work. For this exercise of comparison, we fix the nuisance (calibration) parameters, given in Eq.(2), to be maximally sensitive to any differences between Fisher and MCMC-based constraints for cosmological inference. In contrast to the SNIa case above (see Fig. 5), the MCMC results (filled black contours) agree well with the Fisher predictions (open gray contours), and the resulting posteriors appear Gaussian. The difference in the uncertainties between the two approaches is marginal. We use the same power-spectrum binning scheme, $\Delta_\ell = 100$, for the Fisher forecasts as in the MCMC analysis.

In Fig. 7 we present the results for different power-spectral binning and, like Fig. 7, these correspond to the results for the CMB – S4 survey. The figure shows the ratio of constraints from MCMC with binned spectra to the results obtained for the unbinned ($\Delta_\ell = 1$) spectra using the Fisher formalism: $\Delta_\ell = 50$ in blue, $\Delta_\ell = 100$ in black, and $\Delta_\ell = 200$ in red. We note a mild reduction at 5 – 10% in the constraining power for all parameters for $\Delta_\ell = 100$, our baseline choice. The degradation is less ($\leq 5\%$) for $\Delta_\ell = 50$ but larger (10% – 20%) for $\Delta_\ell = 200$. We emphasize that in this subsection we keep the bin width Δ_ℓ fixed across all angular scales. Although optimal binning strategies tailored to the expected power spectrum can be employed, as is standard for CMB analyses (e.g. T. Louis et al. 2025; E. Camphuis et al. 2025), we do not implement them here. For $\Omega_b h^2$, we obtain a slightly lower constraint for $\Delta_\ell = 200$ compared to $\Delta_\ell = 100$. Although this should not occur in principle, the difference is marginal and consistent with the inherent dispersion in the MCMC process.

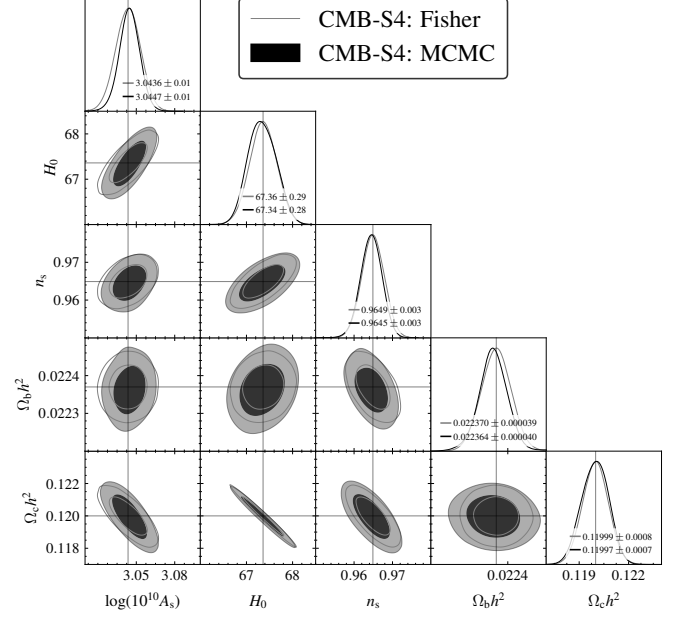


Figure 6. Similar to Fig. 5 but showing the comparison between Fisher-based (open gray contours) constraints and MCMC (filled black contours) for CMB – S4. Unlike SNIa, the CMB posteriors are sufficiently Gaussian, and the differences in the parameter uncertainties are marginal. In both cases, we have adopted our fiducial $\Delta_\ell = 100$ power spectra binning.

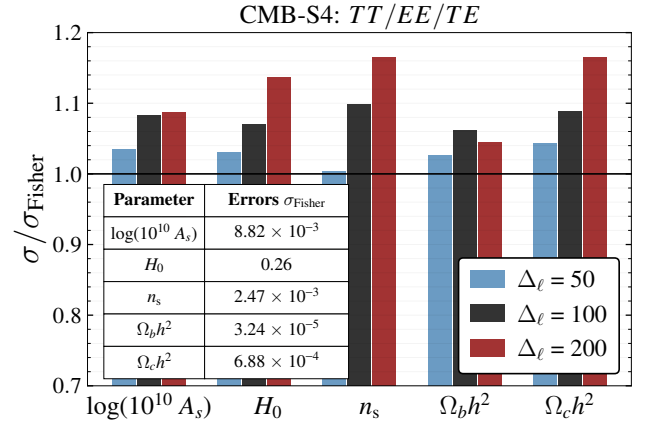


Figure 7. 68% C.L. parameters constraints for the Λ CDM model from the CMB $TT/EE/TE$ power spectra derived using the MCMC sampling for the CMB – S4 survey. The colors represent the constraints for three different binning schemes: $\Delta_\ell = 50$ in blue; $\Delta_\ell = 100$ in black; and $\Delta_\ell = 200$ in red. The bars always correspond to the uncertainties relative to the ones obtained using the Fisher formalism with the unbinned spectra (given in the table). Binning increases the uncertainties of all the parameters by (a) $\leq 5\%$ for $\Delta_\ell = 50$, (b) 5 – 10% for $\Delta_\ell = 100$, which is baseline case; and (c) 10% – 15% for $\Delta_\ell = 200$.

4.4. Dark energy constraints

In Fig. 8, we present the constraints on the dark energy equation of state parameters $\theta \in [w_0, w_a]$. We report both the individual (except for CMB) and some combination of joint constraints from different datasets: LSST-Y3-SNIa, DESI-DR2-BAO, and CMB $TT/EE/TE/\phi\phi$. For reference, we include a table within the figure listing the best-fit values along with their associated uncertainties (68% C.L.).

The orange contours correspond to DESI-DR3-BAO (similar to DESI Collaboration et al. 2025; K. Lodha et al. 2025 for DESI-DR2-BAO); red corresponds to LSST-Y3-SNIa, and teal corresponds to the joint constraints from the two. As listed in the table within in the figure, the uncertainties on w_0, w_a improve by $\sim \times 1.5 - \times 3.5$ from the joint dataset compared to the individual BAO or SNIa results.

We find another $\times 1.5 - \times 2.5$ improvement in both w_0, w_a when the CMB data from SPT-3G (green) is combined with DESI-DR2-BAO and LSST-Y3-SNIa. We also show the combination of LSST-Y3-SNIa and DESI-DR3-BAO with SPT-3G as brown and navy contours. Since the CMB data alone does not constrain w_0, w_a tightly, we do not show the individual constraints for CMB. Throughout this section, we use SPT-3G as the CMB dataset since the constraining power does not differ significantly between CMB datasets. In fact, the uncertainties improve by $\sim < 10\%$ when SPT-3G is replaced by ASO or CMB-S4. This is due to the different direction of degeneracy probed by each of the dataset in the $w_0 - w_a$ plane. For clarity, we show a zoomed-in version of the figure to highlight the improvement in the constraints when SPT-3G is included.

Although DESI-DR3-BAO has a higher individual constraining power on w_a than LSST-Y3-SNIa, as shown by the orange and red contours in Fig. 8, the combination of CMB with LSST-Y3-SNIa yields tighter constraints than CMB with DESI-DR3-BAO. This improvement arises from the nearly orthogonal degeneracy directions in the former combination.

4.4.1. Impact due to extended cosmologies

Next, we investigate the impact on dark energy constraints for other extended cosmologies. In particular, we consider: $w_0 w_a \sum m_\nu$ CDM and $w_0 w_a \Omega_k$ CDM, given the degeneracies between dark energy and spatial curvature or sum of neutrino masses.

In Fig. 9, we present the degradation in $\sigma(w_0)$ and $\sigma(w_a)$ for the extended cosmological models relative to $w_0 w_a$ CDM cosmology, which are explicitly labeled. The plotted values represent the ratio of the current constraints to those obtained for the $w_0 w_a$ CDM model by

combining all the three datasets. The colors indicate different dataset combinations (same as in Fig. 8): brown corresponds to CMB + DESI-DR3-BAO, teal to CMB + LSST-Y3-SNIa, and green to the combination of all three. Similar to Fig. 8, we choose to present only the constraints from SPT-3G here, as the results from other CMB datasets do not show significant differences.

We find that freeing $\sum m_\nu$ has a slightly greater impact on dark energy constraints than freeing spatial curvature Ω_k . Jointly fitting for dark energy with neutrino mass degrades constraints on $\sigma(w_0)$ and $\sigma(w_a)$ by $\sim 10\% - 30\%$ (green bars in the top panel for the $w_0 w_a \sum m_\nu$ CDM model), compared to $< 10\%$ when allowing the Ω_k to vary (green bars in the middle panel for the $w_0 w_a \Omega_k$ CDM model). When both neutrino mass and spatial curvature ($w_0 w_a \sum m_\nu \Omega_k$ CDM model) are allowed to vary, the degradation is roughly similar to the case when only neutrino mass ($w_0 w_a \sum m_\nu$ CDM model) is allowed to vary (green bars in the lower panel). The degradation is more pronounced when CMB is combined only with DESI-DR3-BAO ($\times 2.3 - \times 3$ shown as brown bars in all the panels), than with LSST-Y3-SNIa ($\times 1.7 - \times 1.9$ shown as teal bars), because of the different degeneracy directions as described above.

4.5. Neutrino mass constraints

The sum of neutrino masses, $\sum m_\nu$, has recently gathered significant attention due to a consistent $2-3\sigma$ preference for an unphysical negative value across multiple cosmological datasets that stands in tension with neutrino oscillation experiments (N. Craig et al. 2024; M. Loverde & Z. J. Weiner 2024; D. Green & J. Meyers 2025; G. P. Lynch & L. Knox 2025). Several mechanisms have been proposed to explain this anomaly. For example, excess lensing (A. Cozzumbo et al. 2025), modified value of the optical depth (N. Sailer et al. 2025; W. Elbers 2025) compared to the large-scale polarization measurements from *Planck* (Planck Collaboration et al. 2020a), and modified forms of dark energy (W. Elbers et al. 2025), among others. In this subsection, we forecast the constraints expected from the combination of DESI-DR3-BAO, LSST-Y3-SNIa, and CMB datasets.

In Fig. 10 we present the marginalized constraints for $\sum m_\nu - \Omega_m$ for the $\sum m_\nu \Lambda$ CDM cosmology. Similar to previous figures, we present the constraints individually and for different dataset combinations. In the left panel, the DESI-DR3-BAO only constraints are in orange; the combination of DESI-DR3-BAO with LSST-Y3-SNIa is shown in teal; and further combined with SPT-3G data in green. As shown in the table, including CMB data significantly improves the constraints on $\sum m_\nu$, shifting from no sensitivity to a $\sim 2\sigma$ mea-

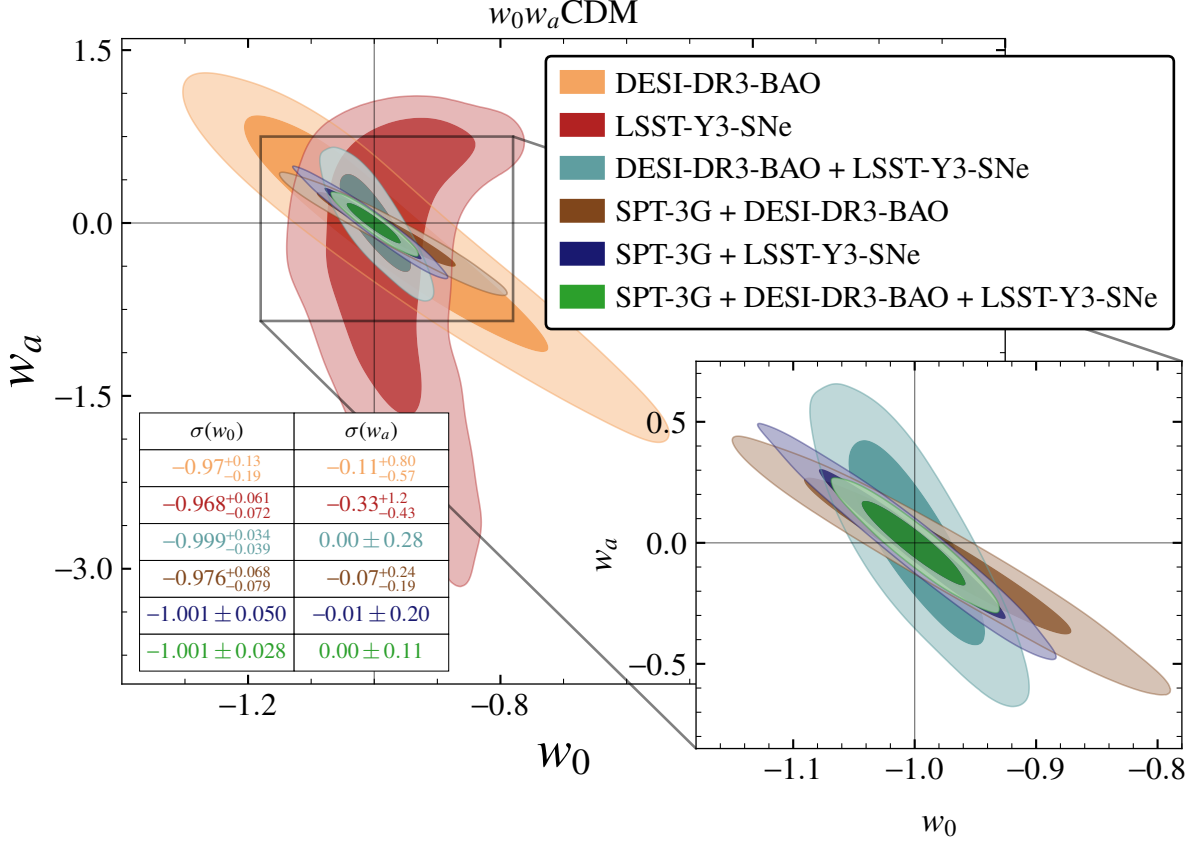


Figure 8. Marginalized constraints on dark energy equation of state parameters for w_0w_a CDM cosmology. The constraints from DESI-DR3-BAO (orange), LSST-Y3-SNIa (red), the combination without (teal) and with (green) CMB $TT/EE/TE/\phi\phi$ data. We also show the constraints when combining DESI-DR3-BAO and LSST-Y3-SNIa individually with SPT-3G in brown and navy contours. The combined constraints shown in green results in $\times 1.5 - \times 2.5$ improvement when the SPT-3G (green) is combined with DESI-DR2-BAO and LSST-Y3-SNIa. We find minimal differences between the choice of CMB dataset as the constraints are primarily driven by the breaking of degeneracies in the $w_a - w_0$ probed by each observable (DESI-DR3-BAO, LSST-Y3-SNIa, and CMB).

surement. This improvement arises from the inclusion of CMB lensing and the differing degeneracy directions between DESI-DR3-BAO and LSST-Y3-SNIa when combined with CMB data. The middle panel illustrates this by showing constraints from various CMB datasets: SPT-3G (green), ASO-Baseline (blue), ASO-Goal (orange), and CMB-S4 (black). In the right panel, we show the joint constraints by combining CMB with LSST-Y3-SNIa and DESI-DR3-BAO for different CMB datasets. While CMB data alone cannot detect $\sum m_\nu$, they significantly tighten the upper limits compared to current surveys (F. Ge et al. 2025; F. J. Qu et al. 2025; E. Camphuis et al. 2025). In contrast, combining CMB data with DESI-DR3-BAO and LSST-Y3-SNIa enables a potential $2 - 3\sigma$ detection of $\sum m_\nu$ assuming a normal hierarchy. Note that these forecast use a *Planck*-like prior on the optical depth to reionization $\sigma(\tau_{\text{re}}) = 0.007$. Unlike for the case of w_0w_a CDM, we see some improvements in the $\sigma(\sum m_\nu)$ constraints for ASO

and $\overline{\text{CMB}} - \overline{\text{S4}}$ compared to SPT-3G due to the reduced lensing bandpower errors resulting from the higher sky fraction for those experiments. This is particularly true for extended cosmologies where $\sum m_\nu$ is left free along with dark energy and/or spatial curvature. For these cases, the constraints degrade by $\times 1.5 - \times 1.8$ for all CMB experiments when combined with LSST-Y3-SNIa and DESI-DR3-BAO datasets as illustrated in Fig. 11.

5. CONCLUSION

In this work, we forecasted the cosmological constraints expected from the combination of upcoming SNIa, CMB, and BAO datasets. Our baseline results were obtained using an MCMC framework. We primarily focused on constraints on dark energy and neutrino masses, adopting a two-parameter extension to Λ CDM for the former and a single-parameter extension for the latter. We also studied the impact of combined extensions involving both dark energy and neutrino mass,

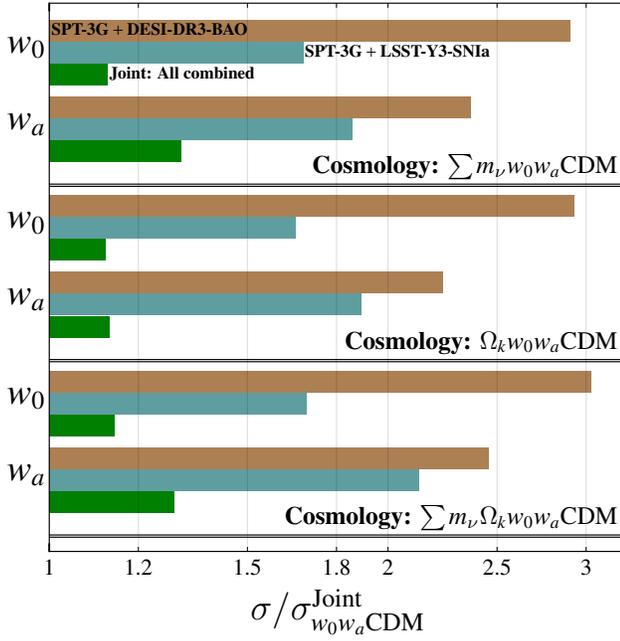


Figure 9. Impact on dark energy equation of state parameters due to extended cosmology scenarios relative to a $w_0 w_a$ CDM cosmology. We present the impact using the ratio of constraints obtained from chains for the extended cosmology scenario under consideration over the ones obtained for $w_0 w_a$ CDM by combining all the three datasets: $\sigma(w_0) = 0.028$ and $\sigma(w_a) = 0.11$ shown using green color in Fig. 8. For the joint dataset, the constraints degrade by $< 10\%$ ($10\% - 30\%$) when jointly fitting dark energy parameters with spatial curvature (neutrino mass).

as well as models that allow for nonzero spatial curvature. Besides the above forecasts, we also (a) compared the improvements moving from the recent DES-Y5-SNIa SNIa sample to LSST-Y3-SNIa, and DESI-DR2-BAO to the upcoming DESI-DR3-BAO release; (b) studied the differences in expected constraints between MCMC and the commonly used Fisher-formalism; and (c) studied the impact of binning the SNIa sample and binning the CMB power spectra. We list our findings below.

- When moving from the recent DES-Y5-SNIa sample to LSST-Y3-SNIa, we found that the uncertainties on both w_0 and w_a are reduced by approximately a factor of $\times 2 - \times 2.5$. This improvement is driven primarily by the substantially increased number density of SNIa in the LSST sample, as well as by the inclusion of objects at $z \geq 1$.
- When swapping the DESI-DR2-BAO measurements with the forthcoming DESI-DR3-BAO, we found a $\times 1.5$ reduction in the uncertainties on both $r_d H_0, \Omega_m$ for Λ CDM cosmology and $\times 1.8$ reduction for w_0, w_a for the $w_0 w_a$ CDM extension.

The majority of this improvement arises from the expanded BAO sample at $z \leq 2$, while clustering measurements of the Ly- α forest at $z > 2$ provide an additional, though smaller, contribution.

- We also found that the traditional Fisher formalism yields overly optimistic constraints and fails to capture the non-Gaussianities in the posterior distribution for SNIa cosmology when using the LSST-Y3-SNIa sample. For the CMB, however, the differences between Fisher forecasts and MCMC-based approaches are only marginal.
- Turning to the impact of binning, we find that binning the SNIa sample following the rebinning approach in (R. Kessler et al. 2023) degrades the uncertainties on (w_0, w_a) by $\sim 30\% - 50\%$. In contrast, for the CMB, binning the power spectra with $\Delta_\ell = 100$ weakens the constraints on all parameters by only $\leq 10\%$ compared to the unbinned case.
- Upon combining CMB data $TT/EE/TE/\phi\phi$ with LSST-Y3-SNIa and DESI-DR3-BAO, we found that we can achieve $w_0 = -0.995 \pm 0.029$ and $w_a = -0.06 \pm 0.11$, with only minor differences across CMB experiments. This represents roughly $\times 6 - \times 8$ ($\times 2 - \times 5$) in $\sigma(w_a)$ ($\sigma(w_0)$) compared to SNIa and BAO datasets individually. When extended cosmologies like neutrino masses $\sum m_\nu$ or spatial curvature Ω_k are considered, the uncertainties on dark energy parameters increase by $\times 1.1 - 1.3$ for the joint datasets. The results are insensitive to the choice of CMB data that is being included.
- The combined DESI-DR3-BAO, LSST-Y3-SNIa, and CMB datasets also can enable a $2 - 3\sigma$ detection of $\sum m_\nu$ assuming a normal Hierarchy depending on the choice of CMB (lensing) dataset that is being considered. *Planck*-like prior on $\sigma(\tau_{\text{re}}) = 0.007$ has been assumed for these forecasts. The sensitivity drops by $\times 1.5 - \times 1.8$ for extended cosmologies that include dark energy and spatial curvature.

As discussed in the text, the improvements in the cosmological constraints will be essential for resolving the mild tensions that have recently emerged, such as the CMB-BAO discrepancy under the assumption of the Λ CDM model. The results presented here are expected to improve further with upcoming data releases, such as DESI-DR4-BAO, DESI-II, and LSST Year-5 and Year-10 supernova samples, as well as through the inclusion

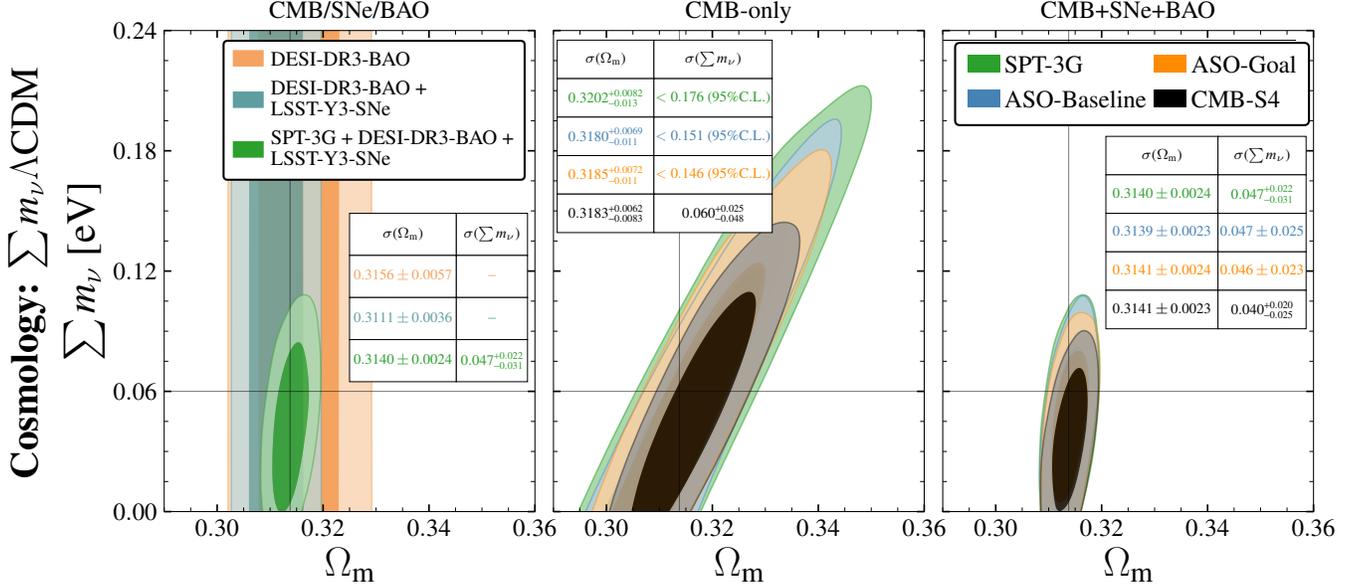


Figure 10. Marginalized constraints on $\sum m_\nu - \Omega_m$ for $\sum m_\nu \Lambda$ CDM cosmology. In the left panel, we show constraints from DESI-DR3-BAO alone in orange; its combination with LSST-Y3-SNIa in teal; and the further combination with CMB from SPT-3G in green. In the middle panel, we show the constraints from various CMB experiments, excluding data from DESI-DR3-BAO and LSST-Y3-SNIa, to highlight the impact of CMB-only measurements. In the right panel, we present the joint constraints obtained by combining CMB with LSST-Y3-SNIa and DESI-DR3-BAO for different CMB datasets. These results indicate that the future datasets can enable to 2 – 3 σ detection of sum of neutrino masses.

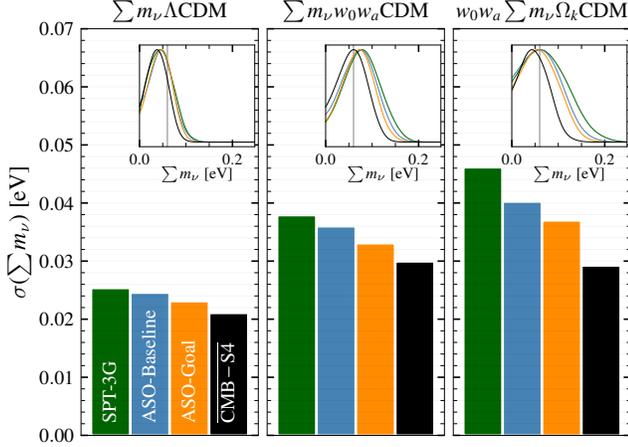


Figure 11. Impact on the constraints on $\sigma(\sum m_\nu)$ due to extended cosmologies: Left panel is for $\sum m_\nu \Lambda$ CDM and it is the same as Fig. 10; middle panel is for $w_0 w_a \sum m_\nu$ CDM; and right panel is for $w_0 w_a \sum m_\nu \Omega_k$ CDM. We note that constraints degrade by $\times 1.5 - \times 1.8$ for the extended cosmologies compared to the left panel. The reported constraints are for the combined CMB, LSST-Y3-SNIa, and DESI-DR3-BAO datasets.

of additional cosmological probes, including the Sunyaev–Zeldovich effects, cluster abundances, $N \times 2$ observables, fast radio bursts, among others (M. S. Madhavacheril et al. 2019; J. Zuntz et al. 2021; Y. Omori et al. 2023; S. Bocquet et al. 2024; M. Glowacki & K.-G.

Lee 2026, for example). These will be further complemented by advancements in survey design for upcoming and next-generation experiments, including SPT-3G+ (A. J. Anderson et al. 2022), CMB-HD (The CMB-HD Collaboration et al. 2022), Nancy Grace Roman Space Telescope (R. Hounsell et al. 2023), the Wide-field Spectroscopic Telescope (WST, V. Mainieri et al. 2024), the all-sky Stage-5 Spectroscopic Survey (Spec-S5, R. Besuner et al. 2025).

DATA PRODUCTS AND AVAILABILITY

The data products and the likelihood codes are publicly available for download and usage in this github link: https://github.com/sriniraghunathan/CMB_BAO_SNe_likelihoods.

ACKNOWLEDGMENTS

SR dedicates this work to the loving memory of Eric Baxter.

We thank Colin Hill for useful discussions about the noise modeling for the Advanced-SO surveys; Brad Benson for feedback on the manuscript; Maciej Bilicki for help with the LSST-DESC publication process; members of the LSST-DESC and SPT collaborations for their valuable discussions throughout the course of this work. This paper has undergone internal review by the LSST-DESC.

Author contributions are listed below: S. Raghunathan: Conceived and led the project and manuscript preparation; A. Mitra: Provided the SNIa sample; N. Šarčević: Assisted with the LSST-DESC products; F. Ge and C. Ravoux: Contributed to the DESI BAO constraints.

SR acknowledges support of Michael and Ester Vaida, and the National Science Foundation via award OPP-1852617; the support by the Illinois Survey Science Fellowship from the Center for AstroPhysical Surveys at the National Center for Supercomputing Applications; and also the support from Universities Research Association’s Visiting Scholars Program fellowship. CG is funded by the MICINN project PID2022-141079NB-C32. IFAE is partially funded by the CERCA program of the Generalitat de Catalunya.

This work made use of the following computing resources: Illinois Campus Cluster, a computing resource that is operated by the Illinois Campus Cluster Program (ICCP) in conjunction with the National Center for Supercomputing Applications (NCSA) and which is

supported by funds from the University of Illinois at Urbana Champaign; and the computing resources provided on Crossover, a high-performance computing cluster operated by the Laboratory Computing Resource Center at Argonne National Laboratory.

The DESC acknowledges ongoing support from the Institut National de Physique Nucléaire et de Physique des Particules in France; the Science & Technology Facilities Council in the United Kingdom; and the Department of Energy, the National Science Foundation, and the LSST Corporation in the United States. DESC uses resources of the IN2P3 Computing Center (CC-IN2P3–Lyon/Villeurbanne - France) funded by the Centre National de la Recherche Scientifique; the National Energy Research Scientific Computing Center, a DOE Office of Science User Facility supported by the Office of Science of the U.S. Department of Energy under Contract No. DE-AC02-05CH11231; STFC DiRAC HPC Facilities, funded by UK BIS National E-infrastructure capital grants; and the UK particle physics grid, supported by the GridPP Collaboration. This work was performed in part under DOE Contract DE-AC02-76SF00515.

APPENDIX

A. COSMOLOGICAL CONSTRAINTS FROM LSST-Y3-SNIa AND DES-Y5-SNIa SAMPLES

In this subsection, we derive the expected cosmological constraints for different subsamples of LSST-Y3-SNIa catalog. As mentioned in the main text (§4.1), this test helps in understanding the improvements in the constraining power when moving from DES-Y5-SNIa to LSST-Y3-SNIa. We summarize the results in Fig. A1. In the figure, the teal contours correspond to DES-Y5-SNIa-mocks (same as in Fig. 3).

In the first case, we assess the improvements provided by the high-redshift SNIa expected in the LSST-Y3-SNIa. For this test, we impose a maximum redshift equal to that of the highest-redshift SNIa in the DES-Y5-SNIa catalog ($z_{\text{max}}^{\text{DES}} \sim 1$). The resulting constraints are shown in red. In this scenario, the constraining power on w_0 and w_a degrades by factors of $\times 1.9$ and $\times 1.6$, respectively, implying that the inclusion of high-redshift objects yields an improvement of roughly 30% – 50%.

In the second case, we construct a SNIa subsample from the full LSST-Y3-SNIa that matches the redshift distribution of the DES-Y5-SNIa catalog. Consequently, this subsample contains approximately the same number of objects as the DES-Y5-SNIa dataset. The resulting

constraints are shown in yellow in Fig. A1, and we note that they are similar to those shown in teal.

Together, these tests show that the factor of $\times 2 - \times 2.5$ improvement in dark energy constraints for the full LSST sample is driven primarily by the increased number of supernovae and partially by the inclusion of high-redshift objects, rather than by calibration improvements.

B. DEPENDENCE OF COSMOLOGICAL CONSTRAINTS ON THE UNDERLYING COSMOLOGICAL MODEL

In this section, we assess how the cosmological constraints depend on the assumed underlying cosmology. As a reminder, throughout this work the fiducial cosmology is taken to be Λ CDM, based on the *Planck* 2018 measurements described in §2.1. Here, we consider two alternative cosmologies motivated by recent results derived from the DES-Y5-SNIa sample. For the first case, we explore an extreme scenario using the inferred values $\Omega_m = 0.495$, $w_0 = -0.36$, and $w_a = -8.8$ from the SNIa-only solution of the DES-Y5-SNIa cosmology analysis (DES Collaboration et al. 2024a). We refer to this model as DES-cosmo. In the second case, we use the updated parameter values from the reanalysis of the DES-Y5-SNIa cosmology incorporating the revised SNIa calibration (B. Popovic et al. 2025), and includ-

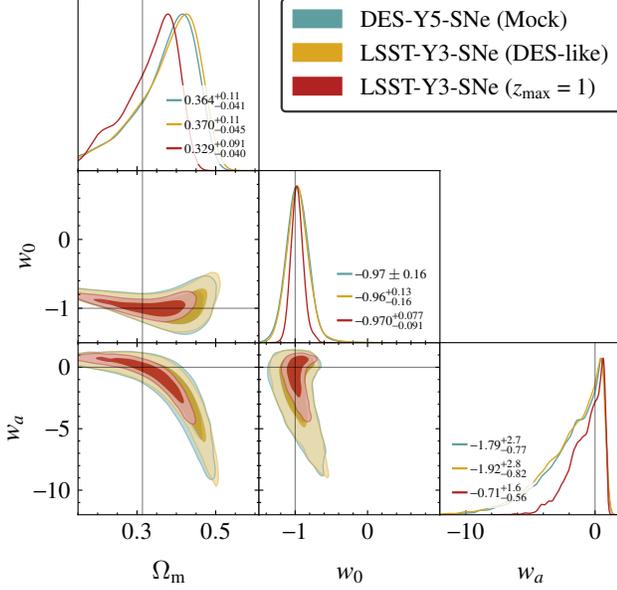


Figure A1. Constraints on dark energy EoS parameters, analogous to Fig. 3, for different subsamples of LSST-Y3-SNIa: yellow contours corresponds to an LSST subsample with the same number counts and redshift distribution as the DES-Y5-SNIa sample; and red contours correspond to the LSST sample with high-redshift SNe removed $z > z_{\text{max}}^{\text{DES}} (\sim 1)$. Teal contours correspond to DES-Y5-SNIa-mocks (same as in Fig. 3); The yellow and teal contours are nearly identical, demonstrating that the reduced calibration uncertainties in the LSST sample alone do not significantly improve the dark energy constraints relative to DES. In contrast, removing the high-redshift SNe (red) weakens the constraints by only about 30–50%. These tests show that the factor of $\times 2 - \times 2.5$ improvement in the dark-energy constraints for the full LSST-Y3-SNIa sample is driven primarily by the larger number of objects relative to the DES-Y5-SNIa sample.

ing CMB and DESI-DR2-BAO. For this model, we set $\Omega_m = 0.33$, $w_0 = -0.803$, and $w_a = -0.72$, and we refer to this cosmology as DES-Dovekie-cosmo. We consider this solution more realistically centred than SNIa-only, where the posterior extends to high values of Ω_m that are outside the bounds of other datasets (for example, cosmic shear). We regenerate the data vectors for both these models.

We present the results in Fig. B2, showing constraints from SNIa-only. In the figure, the original constraints from the DES-Y5-SNIa data-vector are shown as the dash-dotted open teal contours, while the constraints from the mock data vectors assuming the fiducial Λ CDM cosmology are shown as the filled teal contours. These are identical to the results in Fig. 3 and are included here for reference. The constraints for DES-cosmo are

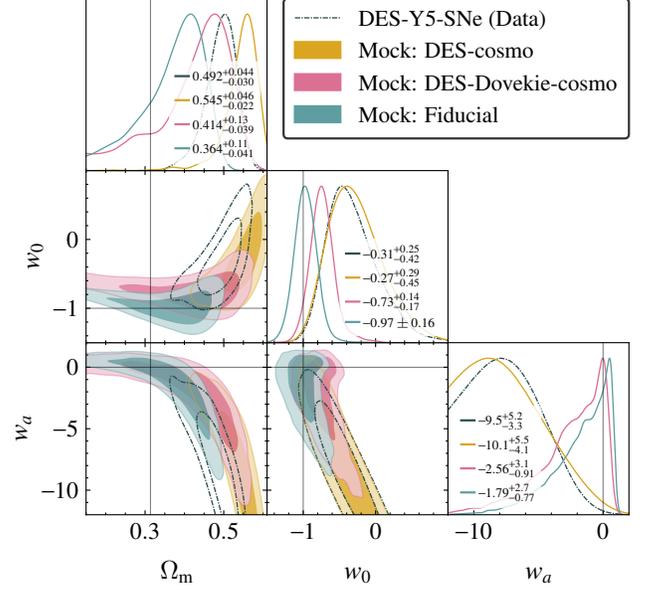


Figure B2. Dependence of the expected cosmological constraints from DES-Y5-SNIa-like SNIa on the underlying cosmology: Open and filled teal contours show the constraints for the original DES data vector and the mock data vector for the fiducial Λ CDM cosmology (same as Fig. 3). The yellow and pink contours correspond to mock data vectors generated assuming DES-cosmo (DES Collaboration et al. 2024a) and DES-Dovekie-cosmo (B. Popovic et al. 2025), respectively. As expected, the constraints for the DES-cosmo mock data (yellow) roughly match the open teal contours. They are, however, significantly weaker than the baseline results, as DES-cosmo probes a different region of the $w_0 - w_a$ posterior volume. In contrast, the DES-Dovekie-cosmo constraints (pink) are only slightly degraded (by $\sim 10\% - 20\%$) relative to the baseline case.

shown in yellow, and those for DES-Dovekie-cosmo are shown in pink.

As seen in the figure, the inferred best-fit values shift to match the assumed underlying cosmology for the yellow and pink contours. We also note that the uncertainties are larger compared to the baseline case (filled teal contours). For DES-cosmo (yellow), the errors worsen significantly —by $\gtrsim \times 2$ for all parameters— relative to the baseline results. These constraints also roughly match those from the original DES analysis (open teal contours), as expected. This arises from the fact that DES-cosmo probes a different region of the $w_0 - w_a$ posterior volume compared to the fiducial case. In contrast, for DES-Dovekie-cosmo (pink), the degradation is much smaller, at the level of only 10%-20% compared to the baseline. While not shown in the figure, we also repeated this test for the joint constraints. In this case, the significant degradation in the constraining power for DES-cosmo disappears for Ω_m , although the trend re-

Table C1. Data vectors for DESI-DR2-BAO computed using the standard Λ CDM cosmology used in this work.

Redshift z	D_V/r_d	D_M/r_d	D_H/r_d
0.295	8.1	-	
0.51	-	13.51	22.8
0.706		17.7	20.2
0.934		22	17.6
1.321		28.1	14.1
1.484		30.3	12.9
2.33		6.6	39.2

mains the same for the dark energy equation-of-state parameters.

C. DESI DATA VECTORS

In Table C1, we list the data vectors generated assuming the standard Λ CDM cosmology for DESI DR2. The covariance matrix is same as the one given in Table 1 of the original DR2 release paper ([DESI Collaboration et al. 2025](#)). Table C2 and Table C3 contain the DESI DR3 data vectors along with the correlations between different observables. The correlations are computed from the covariance matrices released in [DESI Collaboration \(2023\)](#).

REFERENCES

- Abbott, T. M. C., Aguena, M., Alarcon, A., et al. 2022, *PhRvD*, 105, 023520, doi: [10.1103/PhysRevD.105.023520](https://doi.org/10.1103/PhysRevD.105.023520)
- Adame, A. G., Aguilar, J., Ahlen, S., et al. 2025, *JCAP*, 2025, 028, doi: [10.1088/1475-7516/2025/07/028](https://doi.org/10.1088/1475-7516/2025/07/028)
- Alam, S., Ata, M., Bailey, S., et al. 2017, *MNRAS*, 470, 2617, doi: [10.1093/mnras/stx721](https://doi.org/10.1093/mnras/stx721)
- Alam, S., Aubert, M., Avila, S., et al. 2021, *PhRvD*, 103, 083533, doi: [10.1103/PhysRevD.103.083533](https://doi.org/10.1103/PhysRevD.103.083533)
- Anderson, A. J., Barry, P., Bender, A. N., et al. 2022, in *Society of Photo-Optical Instrumentation Engineers (SPIE) Conference Series*, Vol. 12190, Millimeter, Submillimeter, and Far-Infrared Detectors and Instrumentation for Astronomy XI, ed. J. Zmuidzinas & J.-R. Gao, 1219003, doi: [10.1117/12.2629755](https://doi.org/10.1117/12.2629755)
- Aylor, K., Joy, M., Knox, L., et al. 2019, *ApJ*, 874, 4, doi: [10.3847/1538-4357/ab0898](https://doi.org/10.3847/1538-4357/ab0898)
- Balkenhol, L., Dutcher, D., Ade, P. A. R., et al. 2021, *PhRvD*, 104, 083509, doi: [10.1103/PhysRevD.104.083509](https://doi.org/10.1103/PhysRevD.104.083509)
- Bender, A. N., Ade, P. A. R., Ahmed, Z., et al. 2018, in *SPIE Conference Series*, Vol. 10708, Millimeter, Submillimeter, and Far-Infrared Detectors and Instrumentation for Astronomy IX, 1070803, doi: [10.1117/12.2312426](https://doi.org/10.1117/12.2312426)
- Benson, B. A., Ade, P. A. R., Ahmed, Z., et al. 2014, in *SPIE Conference Series*, Vol. 9153, SPIE Conference Series, 1, doi: [10.1117/12.2057305](https://doi.org/10.1117/12.2057305)
- Bernardeau, F. 1997, *Astron. Astrophys.*, 324, 15. <https://arxiv.org/abs/astro-ph/9611012>
- Besuner, R., Dey, A., Drlica-Wagner, A., et al. 2025, arXiv e-prints, arXiv:2503.07923, doi: [10.48550/arXiv.2503.07923](https://doi.org/10.48550/arXiv.2503.07923)
- Bleem, L. E., van Engelen, A., Holder, G. P., et al. 2012, *ApJL*, 753, L9, doi: [10.1088/2041-8205/753/1/L9](https://doi.org/10.1088/2041-8205/753/1/L9)
- Bocquet, S., Grandis, S., Bleem, L. E., et al. 2024, *PhRvD*, 110, 083510, doi: [10.1103/PhysRevD.110.083510](https://doi.org/10.1103/PhysRevD.110.083510)
- Brout, D., Hinton, S. R., & Scolnic, D. 2021, *ApJL*, 912, L26, doi: [10.3847/2041-8213/abf4db](https://doi.org/10.3847/2041-8213/abf4db)
- Caldwell, R. R., & Linder, E. V. 2025, arXiv e-prints, arXiv:2511.07526, doi: [10.48550/arXiv.2511.07526](https://doi.org/10.48550/arXiv.2511.07526)
- Camphuis, E., Quan, W., Balkenhol, L., et al. 2025, arXiv e-prints, arXiv:2506.20707, doi: [10.48550/arXiv.2506.20707](https://doi.org/10.48550/arXiv.2506.20707)
- Cardoso, J.-F., Le Jeune, M., Delabrouille, J., Betoule, M., & Patanchon, G. 2008, *IEEE Journal of Selected Topics in Signal Processing*, 2, 735, doi: [10.1109/JSTSP.2008.2005346](https://doi.org/10.1109/JSTSP.2008.2005346)
- Chevallier, M., & Polarski, D. 2001, *International Journal of Modern Physics D*, 10, 213, doi: [10.1142/S0218271801000822](https://doi.org/10.1142/S0218271801000822)
- CMB-S4 Collaboration. 2019, arXiv e-prints. <https://arxiv.org/abs/1907.04473>
- CMB-S4 Collaboration, Abazajian, K. N., Adshead, P., et al. 2016, ArXiv e-prints. <https://arxiv.org/abs/1610.02743>
- Cozzumbo, A., Atzori Corona, M., Murgia, R., Archidiacono, M., & Cadeddu, M. 2025, arXiv e-prints, arXiv:2511.01967, doi: [10.48550/arXiv.2511.01967](https://doi.org/10.48550/arXiv.2511.01967)
- Craig, N., Green, D., Meyers, J., & Rajendran, S. 2024, *Journal of High Energy Physics*, 2024, 97, doi: [10.1007/JHEP09\(2024\)097](https://doi.org/10.1007/JHEP09(2024)097)

Table C2. The data vectors and the correlations between observables for the low redshift DESI-DR3-BAO data. The data vectors are calculated assuming Λ CDM cosmology, similar to Table C1, and the correlations are computed using the covariance matrices released in (DESI Collaboration 2023).

Redshift z	$f\sigma_8$	D_A/r_d	H_z/r_d	$\rho(f\sigma_8, D_A/r_d)$	$\rho(f\sigma_8, H_z/r_d)$	$\rho(D_A/r_d, H_z/r_d)$
0.05	0.44	1.42	10147.28	0.070	0.103	0.407
0.15	0.46	3.80	10686.55	0.069	0.102	0.407
0.25	0.47	5.68	11294.78	0.068	0.101	0.408
0.35	0.48	7.17	11969.21	0.070	0.104	0.409
0.45	0.48	8.36	12706.62	0.074	0.105	0.409
0.55	0.47	9.29	13503.56	0.073	0.104	0.409
0.65	0.47	10.04	14356.59	0.072	0.102	0.409
0.75	0.46	10.62	15262.39	0.071	0.101	0.410
0.85	0.45	11.08	16217.86	0.071	0.100	0.410
0.95	0.44	11.43	17220.11	0.074	0.103	0.410
1.05	0.43	11.69	18266.54	0.079	0.109	0.411
1.15	0.42	11.89	19354.79	0.073	0.109	0.420
1.25	0.40	12.03	20482.72	0.073	0.109	0.420
1.35	0.39	12.13	21648.43	0.073	0.108	0.420
1.45	0.38	12.18	22850.20	0.073	0.107	0.420
1.55	0.37	12.21	24086.50	0.072	0.105	0.421
1.65	0.36	12.20	25355.95	0.062	0.083	0.414
1.75	0.35	12.18	26657.29	0.061	0.082	0.414
1.85	0.34	12.14	27989.40	0.061	0.081	0.414
1.95	0.33	12.08	29351.27	0.060	0.080	0.414
2.05	0.32	12.01	30741.95	0.059	0.078	0.413

Table C3. Same as Table C2 but for the high redshift measurements expected in DESI-DR3-BAO release.

Redshift z	H_z/r_d	D_A/r_d	$\rho(H_z/r_d, D_A/r_d)$
2.12	31700.38	11.96	0.447
2.28	33991.91	11.82	0.456
2.43	36349.78	11.67	0.461
2.59	38771.20	11.51	0.466
2.75	41254.09	11.34	0.473
2.91	43796.63	11.16	0.474
3.07	46396.73	10.99	0.477
3.23	49053.12	10.81	0.477
3.39	51763.98	10.64	0.479
3.55	54528.16	10.46	0.484

- Dark Energy Survey and Kilo-Degree Survey Collaboration. 2023, The Open Journal of Astrophysics, 6, 36, doi: [10.21105/astro.2305.17173](https://doi.org/10.21105/astro.2305.17173)
- Datta, R., Aiola, S., Choi, S. K., et al. 2018, MNRAS, 2799, doi: [10.1093/mnras/sty2934](https://doi.org/10.1093/mnras/sty2934)
- DES Collaboration, Abbott, T. M. C., Acevedo, M., et al. 2024a, ApJL, 973, L14, doi: [10.3847/2041-8213/ad6f9f](https://doi.org/10.3847/2041-8213/ad6f9f)
- DES Collaboration, Abbott, T. M. C., Acevedo, M., et al. 2024b, ApJL, 973, L14, doi: [10.3847/2041-8213/ad6f9f](https://doi.org/10.3847/2041-8213/ad6f9f)
- DESI Collaboration. 2023, Validation of the Scientific Program for the Dark Energy Spectroscopic Instrument, Zenodo, doi: [10.5281/zenodo.10063934](https://doi.org/10.5281/zenodo.10063934)
- DESI Collaboration, Abdul-Karim, M., Aguilar, J., et al. 2025, arXiv e-prints, arXiv:2503.14738, doi: [10.48550/arXiv.2503.14738](https://doi.org/10.48550/arXiv.2503.14738)
- DESI Collaboration, Aghamousa, A., Aguilar, J., et al. 2016, arXiv e-prints, arXiv:1611.00036, doi: [10.48550/arXiv.1611.00036](https://doi.org/10.48550/arXiv.1611.00036)

- Elbers, W. 2025, arXiv e-prints, arXiv:2508.21069, doi: [10.48550/arXiv.2508.21069](https://doi.org/10.48550/arXiv.2508.21069)
- Elbers, W., Frenk, C. S., Jenkins, A., Li, B., & Pascoli, S. 2025, *PhRvD*, 111, 063534, doi: [10.1103/PhysRevD.111.063534](https://doi.org/10.1103/PhysRevD.111.063534)
- Fang, W., Hu, W., & Lewis, A. 2008, *PhRvD*, 78, 087303, doi: [10.1103/PhysRevD.78.087303](https://doi.org/10.1103/PhysRevD.78.087303)
- Ferraro, S., & Hill, J. C. 2018, *PhRvD*, 97, 023512, doi: [10.1103/PhysRevD.97.023512](https://doi.org/10.1103/PhysRevD.97.023512)
- Ferreira, E. G. M., McDonough, E., Balkenhol, L., et al. 2025, arXiv e-prints, arXiv:2507.12459, doi: [10.48550/arXiv.2507.12459](https://doi.org/10.48550/arXiv.2507.12459)
- Frohmaier, C., et al. 2025, *Astrophys. J.*, doi: [10.3847/1538-4357/adff4e](https://doi.org/10.3847/1538-4357/adff4e)
- Galli, S., Benabed, K., Bouchet, F., et al. 2014, *PhRvD*, 90, 063504, doi: [10.1103/PhysRevD.90.063504](https://doi.org/10.1103/PhysRevD.90.063504)
- Ge, F., Millea, M., Camphuis, E., et al. 2025, *PhRvD*, 111, 083534, doi: [10.1103/PhysRevD.111.083534](https://doi.org/10.1103/PhysRevD.111.083534)
- Giannantonio, T., Fosalba, P., Cawthon, R., et al. 2016, *MNRAS*, 456, 3213, doi: [10.1093/mnras/stv2678](https://doi.org/10.1093/mnras/stv2678)
- Glowacki, M., & Lee, K.-G. 2026, in *Encyclopedia of Astrophysics*, Volume 5, Vol. 5, 448–470, doi: [10.1016/B978-0-443-21439-4.00073-0](https://doi.org/10.1016/B978-0-443-21439-4.00073-0)
- Green, D., & Meyers, J. 2025, *PhRvD*, 111, 083507, doi: [10.1103/PhysRevD.111.083507](https://doi.org/10.1103/PhysRevD.111.083507)
- Gupta, N., Reichardt, C. L., Ade, P. A. R., et al. 2019, *MNRAS*, 490, 5712, doi: [10.1093/mnras/stz2905](https://doi.org/10.1093/mnras/stz2905)
- Guy, J., Astier, P., Baumont, S., et al. 2007, *Astron. Astrophys.*, 466, 11, doi: [10.1051/0004-6361/20066930](https://doi.org/10.1051/0004-6361/20066930)
- Heymans, C., Tröster, T., Asgari, M., et al. 2021, *A&A*, 646, A140, doi: [10.1051/0004-6361/202039063](https://doi.org/10.1051/0004-6361/202039063)
- Hložek, R., Ponder, K. A., Malz, A. I., et al. 2020, arXiv e-prints, arXiv:2012.12392, <https://arxiv.org/abs/2012.12392>
- Hogg, D. W. 1999, arXiv e-prints, astro, doi: [10.48550/arXiv.astro-ph/9905116](https://doi.org/10.48550/arXiv.astro-ph/9905116)
- Hounsell, R., Scolnic, D., Brout, D., et al. 2023, arXiv e-prints, arXiv:2307.02670, doi: [10.48550/arXiv.2307.02670](https://doi.org/10.48550/arXiv.2307.02670)
- Hu, W., & Okamoto, T. 2002, *ApJ*, 574, 566, doi: [10.1086/341110](https://doi.org/10.1086/341110)
- Joudaki, S., Hildebrandt, H., Traykova, D., et al. 2020, *A&A*, 638, L1, doi: [10.1051/0004-6361/201936154](https://doi.org/10.1051/0004-6361/201936154)
- Jungman, G., Kamionkowski, M., Kosowsky, A., & Spergel, D. N. 1996, *PhRvD*, 54, 1332, doi: [10.1103/PhysRevD.54.1332](https://doi.org/10.1103/PhysRevD.54.1332)
- Karwal, T., & Kamionkowski, M. 2016, *PhRvD*, 94, 103523, doi: [10.1103/PhysRevD.94.103523](https://doi.org/10.1103/PhysRevD.94.103523)
- Kessler, R., Cinabro, D., Bassett, B., et al. 2010, *Astrophys. J.*, 717, 40, doi: [10.1088/0004-637X/717/1/40](https://doi.org/10.1088/0004-637X/717/1/40)
- Kessler, R., & Scolnic, D. 2017, *Astrophys. J.*, 836, 56, doi: [10.3847/1538-4357/836/1/56](https://doi.org/10.3847/1538-4357/836/1/56)
- Kessler, R., Vincenzi, M., & Armstrong, P. 2023, *ApJL*, 952, L8, doi: [10.3847/2041-8213/ace34d](https://doi.org/10.3847/2041-8213/ace34d)
- Kessler, R., Narayan, G., Avelino, A., et al. 2019, *Publ. Astron. Soc. Pac.*, 131, 094501, doi: [10.1088/1538-3873/ab26f1](https://doi.org/10.1088/1538-3873/ab26f1)
- Khalife, A. R., Zanjani, M. B., Galli, S., et al. 2024, *JCAP*, 2024, 059, doi: [10.1088/1475-7516/2024/04/059](https://doi.org/10.1088/1475-7516/2024/04/059)
- Knox, L., & Millea, M. 2020, *PhRvD*, 101, 043533, doi: [10.1103/PhysRevD.101.043533](https://doi.org/10.1103/PhysRevD.101.043533)
- Krolewski, A., Ferraro, S., & White, M. 2021, *JCAP*, 2021, 028, doi: [10.1088/1475-7516/2021/12/028](https://doi.org/10.1088/1475-7516/2021/12/028)
- Lewis, A. 2013, *PhRvD*, 87, 103529, doi: [10.1103/PhysRevD.87.103529](https://doi.org/10.1103/PhysRevD.87.103529)
- Lewis, A., Challinor, A., & Lasenby, A. 2000, *ApJ*, 538, 473, doi: [10.1086/309179](https://doi.org/10.1086/309179)
- Lin, M.-X., Raveri, M., & Hu, W. 2019, *PhRvD*, 99, 043514, doi: [10.1103/PhysRevD.99.043514](https://doi.org/10.1103/PhysRevD.99.043514)
- Linder, E. V. 2003, *PhRvL*, 90, 091301, doi: [10.1103/PhysRevLett.90.091301](https://doi.org/10.1103/PhysRevLett.90.091301)
- Lodha, K., Calderon, R., Matthewson, W. L., et al. 2025, *PhRvD*, 112, 083511, doi: [10.1103/w4c6-1r5j](https://doi.org/10.1103/w4c6-1r5j)
- Louis, T., La Posta, A., Atkins, Z., et al. 2025, arXiv e-prints, arXiv:2503.14452, doi: [10.48550/arXiv.2503.14452](https://doi.org/10.48550/arXiv.2503.14452)
- Loverde, M., & Weiner, Z. J. 2024, *JCAP*, 2024, 048, doi: [10.1088/1475-7516/2024/12/048](https://doi.org/10.1088/1475-7516/2024/12/048)
- LSST Dark Energy Science Collaboration. 2012, arXiv e-prints, arXiv:1211.0310, doi: [10.48550/arXiv.1211.0310](https://doi.org/10.48550/arXiv.1211.0310)
- LSST Science Collaboration, Abell, P. A., Allison, J., et al. 2009, arXiv e-prints, arXiv:0912.0201, doi: [10.48550/arXiv.0912.0201](https://doi.org/10.48550/arXiv.0912.0201)
- Lynch, G. P., & Knox, L. 2025, *PhRvD*, 112, 083543, doi: [10.1103/613p-pph2](https://doi.org/10.1103/613p-pph2)
- Madhavacheril, M. S., Battaglia, N., Smith, K. M., & Sievers, J. L. 2019, *PhRvD*, 100, 103532, doi: [10.1103/PhysRevD.100.103532](https://doi.org/10.1103/PhysRevD.100.103532)
- Madhavacheril, M. S., & Hill, J. C. 2018, *PhRvD*, 023534, doi: [10.1103/PhysRevD.98.023534](https://doi.org/10.1103/PhysRevD.98.023534)
- Madhavacheril, M. S., Smith, K. M., Sherwin, B. D., & Naess, S. 2020, arXiv e-prints, arXiv:2011.02475, doi: [10.48550/arXiv.2011.02475](https://doi.org/10.48550/arXiv.2011.02475)
- Madhavacheril, M. S., Qu, F. J., Sherwin, B. D., et al. 2024, *ApJ*, 962, 113, doi: [10.3847/1538-4357/acff5f](https://doi.org/10.3847/1538-4357/acff5f)
- Mainieri, V., Anderson, R. I., Brinchmann, J., et al. 2024, arXiv e-prints, arXiv:2403.05398, doi: [10.48550/arXiv.2403.05398](https://doi.org/10.48550/arXiv.2403.05398)
- Mitra, A., Kessler, R., More, S., & Hložek, R. 2023, *Astrophys. J.*, 944, 212, doi: [10.3847/1538-4357/acb057](https://doi.org/10.3847/1538-4357/acb057)

- Miyatake, H., Sugiyama, S., Takada, M., et al. 2023, *PhRvD*, 108, 123517, doi: [10.1103/PhysRevD.108.123517](https://doi.org/10.1103/PhysRevD.108.123517)
- Namikawa, T., Hanson, D., & Takahashi, R. 2013, *MNRAS*, 431, 609, doi: [10.1093/mnras/stt195](https://doi.org/10.1093/mnras/stt195)
- Nojiri, S., & Odintsov, S. D. 2005, *PhRvD*, 72, 023003, doi: [10.1103/PhysRevD.72.023003](https://doi.org/10.1103/PhysRevD.72.023003)
- Okamoto, T., & Hu, W. 2003, *PhRvD*, 67, 083002, doi: [10.1103/PhysRevD.67.083002](https://doi.org/10.1103/PhysRevD.67.083002)
- Omori, Y., Chown, R., Simard, G., et al. 2017, *ApJ*, 849, 124, doi: [10.3847/1538-4357/aa8d1d](https://doi.org/10.3847/1538-4357/aa8d1d)
- Omori, Y., Baxter, E. J., Chang, C., et al. 2023, *PhRvD*, 107, 023529, doi: [10.1103/PhysRevD.107.023529](https://doi.org/10.1103/PhysRevD.107.023529)
- Ong, D. D. Y., Yallup, D., & Handley, W. 2026, arXiv e-prints, arXiv:2603.05472. <https://arxiv.org/abs/2603.05472>
- Osborne, S. J., Hanson, D., & Doré, O. 2014, *JCAP*, 2014, 024, doi: [10.1088/1475-7516/2014/03/024](https://doi.org/10.1088/1475-7516/2014/03/024)
- Pan, Z., Bianchini, F., Wu, W. L. K., et al. 2023, *PhRvD*, 108, 122005, doi: [10.1103/PhysRevD.108.122005](https://doi.org/10.1103/PhysRevD.108.122005)
- Peloton, J., Schmittfull, M., Lewis, A., Carron, J., & Zahn, O. 2017, *PhRvD*, 95, 043508, doi: [10.1103/PhysRevD.95.043508](https://doi.org/10.1103/PhysRevD.95.043508)
- Planck Collaboration, Aghanim, N., Akrami, Y., et al. 2020a, *A&A*, 641, A6, doi: [10.1051/0004-6361/201833910](https://doi.org/10.1051/0004-6361/201833910)
- Planck Collaboration, Aghanim, N., Akrami, Y., et al. 2020b, *A&A*, 641, A6, doi: [10.1051/0004-6361/201833910](https://doi.org/10.1051/0004-6361/201833910)
- Popovic, B., Brout, D., Kessler, R., Scolnic, D., & Lu, L. 2021, *ApJ*, 913, 49, doi: [10.3847/1538-4357/abf14f](https://doi.org/10.3847/1538-4357/abf14f)
- Popovic, B., Shah, P., Kenworthy, W. D., et al. 2025, arXiv e-prints, arXiv:2511.07517, doi: [10.48550/arXiv.2511.07517](https://doi.org/10.48550/arXiv.2511.07517)
- Poulin, V., Smith, T. L., Karwal, T., & Kamionkowski, M. 2019, *PhRvL*, 122, 221301, doi: [10.1103/PhysRevLett.122.221301](https://doi.org/10.1103/PhysRevLett.122.221301)
- Prabhu, K., Raghunathan, S., Millea, M., et al. 2024, *ApJ*, 973, 4, doi: [10.3847/1538-4357/ad5ff1](https://doi.org/10.3847/1538-4357/ad5ff1)
- Qu, F. J., Ge, F., Kimmy Wu, W. L., et al. 2025, arXiv e-prints, arXiv:2504.20038, doi: [10.48550/arXiv.2504.20038](https://doi.org/10.48550/arXiv.2504.20038)
- Raghunathan, S. 2022, *The Astrophysical Journal*, 928, 16, doi: [10.3847/1538-4357/ac510f](https://doi.org/10.3847/1538-4357/ac510f)
- Raghunathan, S., & Omori, Y. 2023, *ApJ*, 954, 83, doi: [10.3847/1538-4357/ace0c6](https://doi.org/10.3847/1538-4357/ace0c6)
- Reichardt, C. L., Patil, S., Ade, P. A. R., et al. 2021, *ApJ*, 908, 199, doi: [10.3847/1538-4357/abd407](https://doi.org/10.3847/1538-4357/abd407)
- Riess, A. G., Yuan, W., Macri, L. M., et al. 2022, *ApJL*, 934, L7, doi: [10.3847/2041-8213/ac5c5b](https://doi.org/10.3847/2041-8213/ac5c5b)
- Sabogal, M. A., & Nunes, R. C. 2025, arXiv e-prints, arXiv:2505.24465. <https://arxiv.org/abs/2505.24465>
- Sailer, N., Farren, G. S., Ferraro, S., & White, M. 2025, arXiv e-prints, arXiv:2504.16932, doi: [10.48550/arXiv.2504.16932](https://doi.org/10.48550/arXiv.2504.16932)
- Sailer, N., Ferraro, S., & Schaan, E. 2023, *PhRvD*, 107, 023504, doi: [10.1103/PhysRevD.107.023504](https://doi.org/10.1103/PhysRevD.107.023504)
- Sánchez, B. O., Kessler, R., Scolnic, D., et al. 2022, *ApJ*, 934, 96, doi: [10.3847/1538-4357/ac7a37](https://doi.org/10.3847/1538-4357/ac7a37)
- Schaan, E., & Ferraro, S. 2019, *PhRvL*, 122, 181301, doi: [10.1103/PhysRevLett.122.181301](https://doi.org/10.1103/PhysRevLett.122.181301)
- Schöneberg, N., Lesgourgues, J., & Hooper, D. C. 2019, *JCAP*, 2019, 029, doi: [10.1088/1475-7516/2019/10/029](https://doi.org/10.1088/1475-7516/2019/10/029)
- Shaikh, S., Harrison, I., van Engelen, A., et al. 2024, *MNRAS*, 528, 2112, doi: [10.1093/mnras/stad3987](https://doi.org/10.1093/mnras/stad3987)
- Steinhardt, C. L., Phillips, P., & Wojtak, R. 2025, arXiv e-prints, arXiv:2504.03829, doi: [10.48550/arXiv.2504.03829](https://doi.org/10.48550/arXiv.2504.03829)
- Tegmark, M., Taylor, A. N., & Heavens, A. F. 1997, *ApJ*, 480, 22, doi: [10.1086/303939](https://doi.org/10.1086/303939)
- The CMB-HD Collaboration, Aiola, S., Akrami, Y., et al. 2022, arXiv e-prints, arXiv:2203.05728, doi: [10.48550/arXiv.2203.05728](https://doi.org/10.48550/arXiv.2203.05728)
- The Simons Observatory Collaboration, Ade, P., Aguirre, J., et al. 2018, ArXiv e-prints. <https://arxiv.org/abs/1808.07445>
- The Simons Observatory Collaboration, Abitbol, M., Abril-Cabezas, I., et al. 2025, arXiv e-prints, arXiv:2503.00636, doi: [10.48550/arXiv.2503.00636](https://doi.org/10.48550/arXiv.2503.00636)
- Torrado, J., & Lewis, A. 2019, *Cobaya: Bayesian analysis in cosmology*, *Astrophysics Source Code Library*, record ascl:1910.019 <http://ascl.net/1910.019>
- Trendafilova, C. 2023, *JCAP*, 2023, 071, doi: [10.1088/1475-7516/2023/10/071](https://doi.org/10.1088/1475-7516/2023/10/071)
- Vikman, A. 2005, *PhRvD*, 71, 023515, doi: [10.1103/PhysRevD.71.023515](https://doi.org/10.1103/PhysRevD.71.023515)
- Vincenzi, M., Brout, D., Armstrong, P., et al. 2024, *ApJ*, 975, 86, doi: [10.3847/1538-4357/ad5e6c](https://doi.org/10.3847/1538-4357/ad5e6c)
- Vitrier, A., Fichman, K., Balkenhol, L., et al. 2025, arXiv e-prints, arXiv:2510.24669, doi: [10.48550/arXiv.2510.24669](https://doi.org/10.48550/arXiv.2510.24669)
- Zuntz, J., Lanusse, F., Malz, A. I., et al. 2021, *The Open Journal of Astrophysics*, 4, 13, doi: [10.21105/astro.2108.13418](https://doi.org/10.21105/astro.2108.13418)